REPORT DOCUMENTATION PAGE

AFRL-SR-BL-TR-99-

0108

1. AGENCY USE ONLY(Leave blank)	2. REPORT DATE March 29, 1999	3. REPORT TYPE AND DATES COVERED Technical Report (3/1/97-9/30/98)	

4. TITLE AND SUBTITLE

Parallel implicit Multigrid Method for Direct Numerical Simulation of Time-Dependent Compressible Turbulent Flow Around Flight Vehicles

5. FUNDING NUMBERS

6. AUTHOR(S)

Chaoqun Liu, Hua Shan, Li Jiang

7. PERFORMING ORGANIZATION NAME(S) AND ADDRESS(ES)

Department of Mathematics and Statistics
Louisiana Tech University
P.O.Box 3189
Ruston, LA 71272

8. PERFORMING ORGANIZATION REPORT NUMBER

9. SPONSORING/MONITORING AGENCY NAME(S) AND ADDRESS(ES)

AIR FORCE OFFICE OF SCIENTIFIC RESEARCH
Directorate of Aerospace Science
801 North Randolph Street
Arlington, VA 22203-1977

10. SPONSORING/MONITORING AGENCY REPORT NUMBER

11. SUPPLEMENTARY NOTES

19990414007

12a. DISTRIBUTION/AVAILABILITY STATEMENT

APPROVED FOR PUBLIC RELEASE
DISTRIBUTION IS UNLIMITED

12b. DISTRIBUTION CODE

13. ABSTRACT

An oblique transition process of a flat-plate boundary layer at a free-stream Mach number of M_∞ =4.5 and a Reynolds number of 10000 based on free-stream velocity and inflow displacement thickness is simulated as the validation of the code. Four transitional stages are observed: the linear and weakly nonlinear growth, the appearance of staggered Λ-vortex patterns, the evolution of Λ-vortex into hairpin vortex, the breakdown of hairpin vortical structures. The evolution of averaged quantities, such as the skin-friction coefficient, the mean velocity profile, the boundary layer thickness are all computed and found agreed very well with theoretic and experimental results. For complex geometry, 2D and 3D numerical grid generation method are used to generate high-quality meshes. Subsonic flow around 2D NACA 0012 airfoil and 3D Delta wing with a large angle of attack are investigated with large eddy simulation. Flow separations and large eddy structures are observed, the interactions between vortical structures will be studied.

14. SUBJECT TERMS

Large Eddy Simulation; Transition; Compressible; Three-dimensional; Navier-Stokes; Boundary Layer;

15. NUMBER OF PAGES

42

16. PRICE CODE

17.SECURITY CLASSIFICATION OF REPORT	18. SECURITY CLASSIFICATION OF THIS PAGE	19. SECURITY CLASSIFICATION OF ABSTRACT	20. LIMITATION OF ABSTRACT
Unclassified	Unclassified	Unclassified	

DTIC QUALITY INSPECTED 4

Parallel Implicit Multigrid Method for Direct Numerical Simulation of Time-Dependent Compressible Turbulent Flow Around Flight Vehicles [*]

C. Liu[†],   H. Shan[‡],   L. Jiang[§]

Center for Numerical Simulation and Modeling
College of Engineering and Science, Louisiana Tech University
P.O. Box 10348
Ruston, LA 71272, U.S.A.

[†]Professor of Mathematics
[‡]Post-doctoral Research Associate
[§]Post-doctoral Research Associate

Chapter 1

Code Validation: Numerical Simulation of Flow Transition in a Mach 4.5 Flat-Plate Boundary Layer

1.1 Introduction

Recent advances in supersonic and hypersonic aerospace technology have revived the interest in boundary layer transition for high Mach number flows. A thorough understanding, prediction, and control of boundary layer transition at high Mach number is crucial in the design of aerodynamic vehicles. For example, skin friction and aerodynamic heating are considerably lower for laminar flows at high speed than turbulent flow. However, the mechanism of transition in high speed boundary layer is still poorly understood. On the contrary to a relatively comprehensive picture of transition scenarios in incompressible flows, nonlinear effects responsible for transition at high speed are still very much a mystery (Erlebacher & Hussaini, 1990). Owing to the enormous difficulties of controlled experiments for high-supersonic flows, experimental results revealing detailed flow phenomena at the nonlinear stage of supersonic transition are hardly found in literature. Instead, they have been mostly restricted to the domain of linear disturbance growth. Because of lack of experimental data there is a strong interest in numerical simulation techniques for studying transition, direct numerical simulation (DNS) and large eddy simulation (LES) are now major tools to play an important role on providing understandings to high-speed flow transition.

The investigation of supersonic transition by experimental measurement has been proved to be very difficult. Uncertainty of data obtained using hot-wire anemometry is considerably higher than that obtained in subsonic flow. It is also very difficult to obtain accurate measurement near the wall due to lack of spatial resolution. Alternatively, the investigation can be launched through theoretical and computational study.

The theoretical and computational tools for analysis of stability and transition include: compressible linear stability theory (LST)(Mack, 1984); secondary instability theory (SIT) (Herbert, 1988; Ng & Erlebacher, 1991); parabolized stability equation (PSE) methods (Herbert & Bertolotti, 1987; Chang & Malik, 1993); temporal direction numerical simulation (DNS) (Erlebacher & Hus-

saini, 1990; Pruett & Zang, Adams & Kleiser, 1996); spatial DNS (Thumm *et al.*, 1990; Pruett *et al.*, 1995a, 1995b); temporal large eddy simulation (LES) (El-Hady & Zang, 1995); spatial LES (Ducros *et al.*, 1996);

In the linear stability theory, the base flow is assumed to be parallel in the streamwise direction. The Navier-Stokes equations are linearized by formulating the disturbance quantities in the normal mode form. This leads to a set of ordinary differential equations. The system has been transformed to an eigenvalue problem. The first-mode instability is analogour to the T-S instability in incompressible flow. At $Ma > 3.8$, the first-mode instability is purely inviscid(Pruett *et al*, 1991). Unlike T-S instability, the first-mode instability in supersonic flow are most unstable when oblique, while in incompressible flow, according to Squire's theorem the two-dimensional mode is more unstable than the three dimensional mode.

In the secondary instability theory, the base flow is defined as the sum of mean flow and the superimposed primary instability wave. Onset of secondary instability is quite sensitive to the amplitude of the imposed primary disturbance. There are three types of secondary instability: fundamental (K-type), detuned, and subhamonic (H-type). At large primary amplitude, the fundamental secondary instability is more favored(Pruett *et al*, 1991), where the Λ-shaped vortices are aligned along their peaks in the streamwise direction, repeating every primary wavelength. Small to moderate amplitudes of the primary disturbance often bring out the subharmonic secondary instability (Pruett *et al*, 1991), where the Λ-shaped vortices are staggered in the streamwise direction, repeating at a distance equal to twice the primary wavelength. The situation of detuned instability is between the fundamental and the subharmonic one.

In the parabolized stability equations (PSE) approach (Herbert & Bertolotti, 1987), one attempts to construct an approximate solution of the full Navier-Stokes equations, where the nonparallel effects are taken into account. Though the parabolized stability equation method can be served as an alternative for DNS in some range, the cost of PSE increase much faster than that of DNS as the number of spanwise modes increases. Therefore, PSE is limited in practice to investigations of narrow-band focing (Pruett *et al.*, 1995a).

The compressible linear stability theory (LST), the secondary instability theory (SIT), and the parabolized stability equation (PSE) methods can only provide limited information for flow transition, and they are far away from practical application.

Direct numerical simulation is a technique that all the flow scales are accurately resolved. DNS of flat-plate boundary layers over a wide range of Mach numbers (e.g., up to Mach 8 or higher) have resulted in some encouraging quantitative comparisons accurate to several digits with theories (Pruett *et al.*, 1995a). However, being limited by the capacity of modern computers, most DNS are limited to temporal simulation of transition, in which a spatially periodic computational domain travels with the disturbance and the temporal evolution of the disturbance is computed. This enabled simulations into the later stages of transition (Zang & Hussaini, 1990; Laurien & Kleiser, 1989; Pruett & Zang, 1992). A temporal subharmonic transition in a Mach 4.5 flat-plate boundary

layer has been simulated successfully by Adams & Kleiser (1996) using direct numerical simulation. An approach has been developed by Liu *et al*, (1996a, 1996b) to simulate the whole process of transition in the incompressible boundary layer of flat-plate and of airfoils. For compressible flow, some of the techniques from their previous works. are combined with the explicit schemes, which is efficient especially for supersonic flow with high Mach numbers. In addition, the explicit code is easy to be vectorized and parallelized. With this approach, the spatial transition of boundary layer flow of flat-plate and airfoil is investigated by direct numerical simulation (Zhao *et al*, 1997). However, the computational cost is high and the skin-friction coefficients and velocity profile are not accurate for fully developed turbulent flow.

Large eddy simulation (LES) is a technique that has been successfully applied to the study of turbulent flows, and has become a very important method of simulation. In LES only the large energy-carrying scales are resolved, while the influence of small or subgrid scales must be modeled appropriately. A filtering process is usually used to separate the large- and small-scale motions, large-scale structures are resolved by the filtered equations, but a model is employed to formulate the contributions from the subgrid-scale fluctuations, such as the subgrid scale stress and heat flux terms. Compared with DNS, LES is more affordable at present stage. LES is capable to solve problems with complex geometry using spatial approach(Berlin, 1994; Ducros *et al.*, 1996).

In the present work, the spatial transition of a Mach 4.5 flat-plate flow is investigated by LES. A pair of oblique first-mode perturbation is imposed on the inflow boundary. The numerical method is based on the three-dimensional time-dependent compressible Navier-Stokes equations in the curvilinear coordinate system. A compact sixth-order central difference scheme(Lele, 1992) is applied to the wall-normal direction and streamwise direction. In the spanwise direction, the pseudo-spectral method is used based on the assumption that the periodic condition is satisfied. The compact storage third order Runge-Kutta scheme (Wray, 1986) is applied for time-integration. The similar approach has been used by us (Zhao *et al*, 1997) in direct numerical simulation. The major objective of this work focus on the LES of supersonic flow. The numerical results that are comparable to the DNS are obtained by LES with less grid numbers and less CPU-hours. In the present work, the filtered structure function model (Ducros *et al.*, 1996) is adopted.

The paper is organized as follows. Section 2 contains the governing equations and the LES model. In Section 3, some of the computational details are presented. The computational results and discussion are in Section 4.

1.2 Mathematic Model

1.2.1 Governing Equations

In large eddy simulation of fluid flow the large scale structures are simulated exactly while the effect of the small scale structures is modeled. The large scales are extracted from the dependent

variables by applying a filtering operation to the continuity, the Navier-Stokes, and the energy equations. To account for large density fluctuations in high-speed compressible flows, the Favre-filtering operation is employed, where the resolved velocity and temperature fields are written in terms of Favre-filtered quantities, which are defined as

$$\tilde{F} = \frac{\overline{\rho F}}{\overline{\rho}} \tag{1.1}$$

where the "—" denotes the spatial filtering. The nondimensional Favre-filtered governing equations of continuity, momentum, and temperature are described as follows:

$$\frac{\partial \overline{\rho}}{\partial t} + \frac{\partial}{\partial x_k}(\overline{\rho}\tilde{u}_k) = 0 \tag{1.2}$$

$$\frac{\partial \overline{\rho}\tilde{u}_k}{\partial t} + \frac{\partial}{\partial x_l}(\overline{\rho}\tilde{u}_k\tilde{u}_l) = -\frac{\partial \overline{p}}{\partial x_k} + \frac{1}{Re}\frac{\partial \tilde{\sigma}_{kl}}{\partial x_l} + \frac{\partial \tau_{kl}}{\partial x_l} \tag{1.3}$$

$$\frac{\partial \overline{\rho}\tilde{T}}{\partial t} + \frac{\partial}{\partial x_k}\left(\overline{\rho}\tilde{u}_k\tilde{T}\right) = -\gamma(\gamma-1)M_\infty^2 \overline{p}\frac{\partial \tilde{u}_k}{\partial x_k} + \frac{\gamma(\gamma-1)M_\infty^2}{Re}\tilde{\sigma}_{kl}\frac{\partial \tilde{u}_k}{\partial x_l} + \frac{\partial}{\partial x_k}(\frac{\gamma\tilde{\mu}}{PrRe}\frac{\partial \tilde{T}}{\partial x_k}) + \frac{\partial q_k}{\partial x_k} \tag{1.4}$$

where ρ is the density, u_k is the velocity component in the kth direction, p is the pressure, and T is the temperature. The viscous stress is

$$\tilde{\sigma}_{kl} = \tilde{\mu}\left[\left(\frac{\partial \tilde{u}_k}{\partial x_l} + \frac{\partial \tilde{u}_l}{\partial x_k}\right) - \frac{2}{3}\frac{\partial \tilde{u}_m}{\partial x_m}\delta_{kl}\right] \tag{1.5}$$

In the nondimensionalization, the reference values for length, density, velocity, and temperature are δ_{in}, ρ_∞, U_∞, and T_∞, respectively. δ_{in} is the displacement thickness of inflow. The Mach number, the Reynolds number, the Prandtl number, and the ratio of specific heats, are defined respectively as follows:

$$M_\infty = U_\infty\left(\gamma R T_\infty\right)^{-1/2}, \quad Re = \frac{\rho_\infty U_\infty \delta_{in}}{\mu_\infty}, \quad Pr = \frac{C_p \mu_\infty}{\kappa_\infty}, \quad \gamma = \frac{C_p}{C_v}$$

where R is the ideal gas constant, C_p and C_v are the specific heats at constant pressure and constant volume. Through this work, $Pr = 0.7$, and $\gamma = 1.4$. The viscosity is determined according to Sutherland's law, in dimensionless form

$$\mu = \frac{T^{3/2}(1+S)}{T+S}, \quad S = \frac{110.3K}{T_\infty}$$

In Eq.(1.3) and (1.4), the subgrid scale stress and heat flux are denoted by

$$\tau_{kl} = -\overline{\rho}\left(\widetilde{u_k u_l} - \tilde{u}_k\tilde{u}_l\right) \tag{1.6}$$

$$q_k = -\overline{\rho}\left(\widetilde{u_k T} - \tilde{u}_k\tilde{T}\right) \tag{1.7}$$

which are needed to be modeled.

1.2.2 Filtered Structure Fuction Model

The filtered structure-function model is developed by Ducros *et al.* (1996). The subgrid scale shear stress and heat flux can be modeled as

$$\tau_{kl} = \overline{\rho}\nu_t \left[\left(\frac{\partial \tilde{u}_k}{\partial x_l} + \frac{\partial \tilde{u}_l}{\partial x_k} \right) - \frac{2}{3}\frac{\partial \tilde{u}_m}{\partial x_m}\delta_{kl} \right] \tag{1.8}$$

$$q_k = \frac{\gamma\overline{\rho}\nu_t}{Pr_t}\frac{\partial \widetilde{T}}{\partial x_k} \tag{1.9}$$

Here, Pr_t is the turbulent Prandtl number taken equal to 0.6 as in isotropic turbulence, ν_t is the turbulent kinetic viscosity defined as

$$\nu_t(x,t) = 0.0014 C_K^{-3/2}\Delta \left[\tilde{F}_2^{(3)}(x,t) \right]^{1/2} \tag{1.10}$$

where $\tilde{F}_2^{(3)}$ is the filtered structure function. In the case of flat-plate boundary layer flows with meshes flattened in the wall-normal direction, $\tilde{F}_2^{(3)}$ takes the four-neighbor formulation proposed by Normand & Lesieur (1992).

$$\tilde{F}_2^{(3)} = \frac{1}{4}\left[\left\|\tilde{u}_{i+1,j}^{(3)} - \tilde{u}_{i,j}^{(3)}\right\|^2 + \left\|\tilde{u}_{i-1,j}^{(3)} - \tilde{u}_{i,j}^{(3)}\right\|^2 + \left\|\tilde{u}_{i,j+1}^{(3)} - \tilde{u}_{i,j}^{(3)}\right\|^2 + \left\|\tilde{u}_{i,j-1}^{(3)} - \tilde{u}_{i,j}^{(3)}\right\|^2 \right] \tag{1.11}$$

where

$$\tilde{u}_{i,j}^{(3)} = HP^{(3)}(\tilde{u}_{i,j})$$

$\Delta = (\Delta_x\Delta_y)^{1/2}$ is used to characterize the grid size. C_K is the Kolmogorov constant taking the value of 1.4. $HP^{(3)}$ is a discrete Laplacian filter iterated 3 times, which is served as a high-pass filter before computing the structure function. The first iteration of the Laplacian filter $HP^{(1)}$ is defined by

$$\tilde{u}_{i,j}^{(1)} = HP^{(1)}(\tilde{u}_{i,j}) = \tilde{u}_{i+1,j} - 2\tilde{u}_{i,j} + \tilde{u}_{i-1,j} + \tilde{u}_{i,j+1} - 2\tilde{u}_{i,j} + \tilde{u}_{i,j-1} \tag{1.12}$$

1.2.3 Boundary Conditions

Non-slip boundary condition for velocity components is imposed on the wall, where an adiabatic condition is also sited. The inflow condition is composed of the two-dimensional Blasius-like profile resulting from the resolution of the similarity equation and a pair of oblique first-modes, as it will be described in detail in next section. At the far-field boundary, we adopt the nonreflecting boundary condition proposed by Thompson(1987). A sponge section occupying 2 primary wavelengths in the streamwise direction is settled near the outflow boundary, which is similar to the sponge condition used by Collis & Lele(1996). A source term is added to the right hand side of equations as

$$W(Q) = -f_d(x)(Q)$$

where the sponge function is given by

$$f_d(x) = \begin{cases} A_s \left(\frac{x - x_s}{x_o - x_s} \right)^{N_s} & x \in (x_s, x_o] \\ 0 & \text{otherwise} \end{cases}$$

where x_s and x_o stand for the streamwise coordinate of the starting and ending points of the sponge section, respectively. A_s and N_s are used to control the amplitude and strength of the sponge function. Here, $A_s = 10$ and $N_s = 3$ are set.

1.3 Computational Procedure

The numerical simulation is performed using a spatial approach to solve a full compressible Navier-Stokes system in the curvilinear coordinates. A compact sixth-order central difference scheme (Lele, 1992) is applied to the wall-normal direction and streamwise direction, the pseudo-spectral method is used in the spanwise direction. The compact storage third order Runge-Kutta scheme (Wray, 1986) is adopted for time-integration. The computational domain is displayed in Figure 1.1. We designate x as the streamwise direction, y as the spanwise direction, and z as the wall-normal direction. The flow parameters and computational details have been collected in Table 1.1, where the inflow displacement thickness is denoted by δ_{in}, x_{in} is defined as the distance between the leading edge of the flat-plate and the upstream boundary of the computational domain. The Reynolds number is based on the displacement thickness at the inflow boundary and the free-stream velocity.

The computation domain covers a streamwise region between $x = 91.33\delta_{in}$ and $x = 510.21\delta_{in}$, thus a streamwise dimension of $L_x = 418.88\delta_{in}$, which equals to 32 streamwise primary wavelength λ_x. The spanwise dimension is $L_y = 7.57\delta_{in}$ covering 1 spanwise primary wavelength λ_y. The wall-normal dimension at the upstream boundary is $22\delta_{in}$. The number of grid points in each direction is $N_x = 1024$, $N_y = 33$, and $N_z = 61$, respectively. The grid, uniformly distributed in the streamwise and spanwise direction, is stretched from the wall in the wall-normal direction.

A pair of the most unstable oblique first modes with wave-number of (1,1) and (1,-1) and equal amplitude are imposed as the inflow perturbation. The frequency of the disturbance is $\omega = 0.3878$. The streamwise and spanwise wavenumbers are $\alpha_r = 0.48$ and $\beta = 0.83$ respectively, corresponding to the streamwise and spanwise wavelength of 13.09 and 7.57, thus the oblique angle is 60°. The maxima of the streamwise velocity disturbance amplitude is about 2% of U_∞.

The time step is set to be 0.0162 (1000 time steps are used per period of the forced perturbation). With the number of grid points listed in Table 1.1, the CPU time of each time step is 8.2 seconds running on a single processor of Cray-T90. For this simulation we used 30000 time steps which amounts to 70 CPU hours.
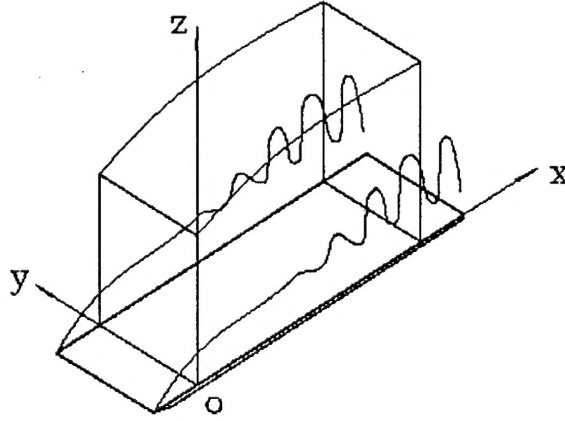
6

Figure 1.1: Computational domain of flat-plate boundary layer flow

1.4 Results and Discussion

1.4.1 Mean flow behavior

In this section, the characteristics of the mean flow is discussed. The Fourier transformation is carried out in time- and spanwise-direction to obtain spectral components (k_t, k_y) in Fourier space, where k_t and k_y stand for the temporal and spanwise wavenumbers, respectively. The mean flow is characterized by the spectral component $(0, 0)$.

The skin friction coefficient calculated from the time- and spanwise-averaged velocity profile is displayed in Figure 1.2. The spatial evolution of skin friction coefficient of laminar flow is also plotted out for comparison. It is observed from this figure that the sharp growth of the skin-friction coefficient occurs after $x \approx 180\delta_{in}$ (i.e. $Re_x = 1.8 \times 10^6$), which will be defined as the 'transition point'. The skin friction coefficient after transition is in good agreement with the flat-plate theory of turbulent boundary layer by Van Driest(1956).

The thickness of boundary layer obtained from the simulation has been plotted in Figure 1.3. The boundary layer thickness are calculated based on the time- and spanwise-averaged velocity profile. The boundary layer thickness is defined as the distance from the wall where the mean velocity reaches 99% of the free-stream velocity. A sudden growth in the boundary layer thickness after $x \approx 200\delta_{in}$ is observed as a result of the transition to turbulence. No sudden adjustment can be observed from the curve of the displacement thickness and momentum thickness.

Time- and spanwise-averaged streamwise velocity profiles for various fixed values of the streamwise coordinate $x = 91.33\delta_{in}$, $221.63\delta_{in}$, $243.38\delta_{in}$, $265.13\delta_{in}$ and $286.88\delta_{in}$ are shown in Figure 1.4. The inflow velocity profile at $x = 91.33\delta_{in}$ is of a typical laminar flow. Starting from $x = 243.38\delta_{in}$, the mean velocity profiles resemble that of turbulent flow.

7

M_∞	4.5
$Re = \frac{\rho_\infty U_\infty \delta_{in}}{\mu_\infty}$	1.0×10^4
Pr	1.0
δ_{in}	inlet displacement thickness
x_{in}	$91.33\delta_{in}$
T_∞^*	$61.11K$
T_w^*	$267.66K$ ($T_w = 4.38$)
ω	0.3878
β	0.83
α_r	0.48
α_i	-1.35586×10^{-2}
$\lambda_x = \frac{2\pi}{\alpha_r}$	13.09
$\lambda_y = \frac{2\pi}{\beta}$	7.57
L_x	$418.88\delta_{in}$
L_y	$7.57\delta_{in}$
L_{zin}	$22.0\delta_{in}$
$Grids : N_x \times N_y \times N_z$	$1024 \times 33 \times 61$

Table 1.1: Flow parameters and computational details

In Figure 1.5, we show the time- and spanwise-averaged velocity profile, plotted in terms of logarithm scaled wall unit, where the friction velocity and the friction length are defined as $u_\tau = (\tau_w/\rho_w)^{1/2}$ and $z_\tau = \frac{\mu_w}{Re\rho_w u_\tau}$, respectively. The linear law near the wall has been marked by the cross symbol. The log law curves of both incompressible and compressible turbulent flow are also plotted as comparison. The wall law of compressible turbulent flow displayed here is based on the effective velocity concept of van Driest (1951) and the first-order theoretical law of wall given by White and Christoph (1972). Actually the curves of two theories coincide very well, one can hardly distinguish them from each other on this figure. There is evidently a log region on the profile at $x = 243.38\delta_{in}$, from where the mean velocity profile resembles that of fully developed turbulent flow, see also Figure 1.4. In the log region, our results are in good agreement with the theory of Van Driest(1951) and White & Christoph(1972). The lower of the velocity profile, in the log range, compared with that of incompressible turbulent flow, can be explained as the effect of compressibility.

1.4.2　Linear and nonlinear disturbance evolution

In Figure 1.6, we show the maxima amplitude of streamwise velocity perturbation of selected modes as a function of streamwise coordinate. The wavenumbers of these modes are denoted as (k_t, k_y), where k_t refers to the temporal wavenumber, k_y is the spanwise wavenumber. Here and after, the
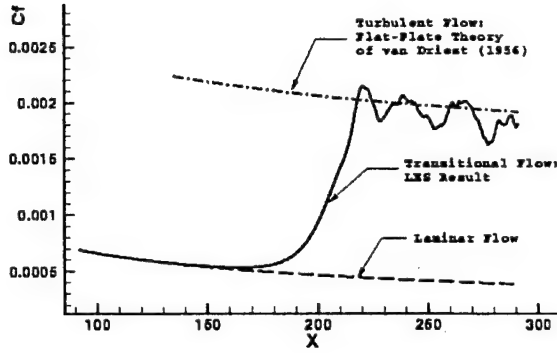
8

Figure 1.2: Streamwise evolution of skin-friction coefficient obtained from the time- and spanwise-averaged streamwise velocity profile
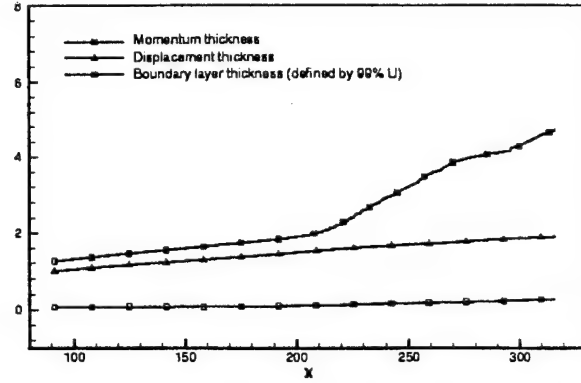

Figure 1.3: Thickness of boundary layer as a function of streamwise coordinate

modes with an even sum of $k_t + k_y$ are called the even modes, those with an odd sum of $k_t + k_y$ are termed as the odd modes. In Figure 1.6, the even modes are plotted with solid line, and the odd modes with dashed lines. It is apparent from the figure that the disturbance growth is dominated by even modes.

As can be seen from Figure 1.6, at the inflow boundary ($x = 91.33\delta_{in}$), the superimposed primary wave (1,1)-mode is visibly well standing out above all other modes. Before $x \approx 170\delta_{in}$, the (1,1)-mode grows with its linear growth rate, which is approximately $\alpha_i = -1.35 \times 10^{-2}$. The linear growth of the primary wave covers almost 6 primary wavelength in the streamwise direction. It is noticeable that the (0,2)-mode is rapidly amplified and it overtakes the primary wave mode at $x \approx 150\delta_{in}$. Since the primary wave is composed of a pair of oblique modes (1,1) and (1,−1), the weakly nonlinear interaction of the oblique couple can excite the (0,2)and (2,0)-modes. The further interaction of (1,1),(1,-1),(0,2),(2,0)-modes results in the generation of (1,3),(3,1),(2,2),(3,3),(0,4),(4,0),(2,4),(4,2)-modes, etc. Thus, the weakly nonlinear interaction among the even modes can only excite the even modes. The sharp growth of the odd modes, which are evoked by the strong nonlinear interaction, is observed after $x \approx 150\delta_{in}$. It is also very interesting to see that the linear growth of primary wave extends into the nonlinear region. At far downstream, both the even modes and the odd modes are saturated, as the maxima amplitude of velocity perturbation stays near a certain level.

The linear and nonlinear disturbance growth before $x \approx 180\delta_{in}$ can be regarded as the first stage of transition. Up to this point, because the amplitude of disturbance is too small to make evident change to the mean flow velocity profile, the skin-friction coefficient stays at its laminar flow value. The study of the growth of separated Fourier spectral modes may provide some insights into the description of organized motion during the transition process, as it will be described in
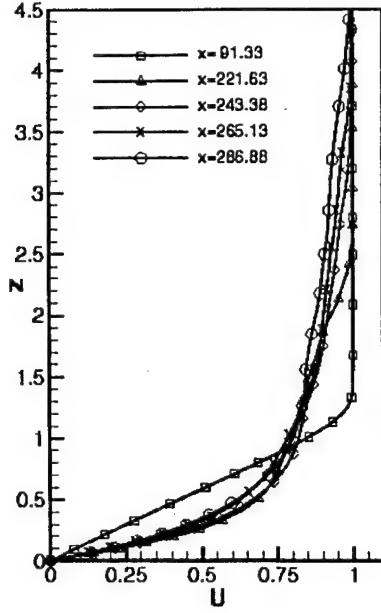
9

Figure 1.4: Time- and spanwise-averaged streamwise velocity profiles at different streamwise locations
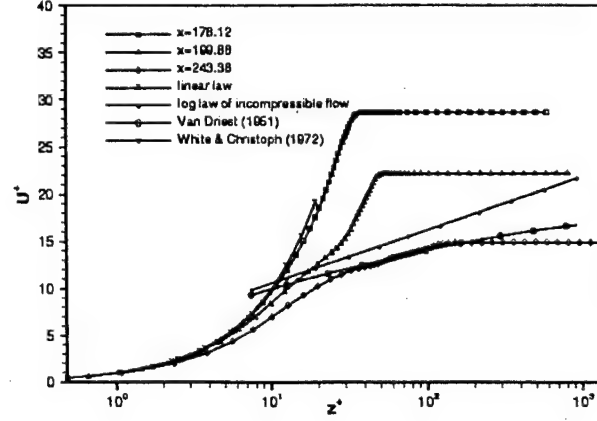

Figure 1.5: Log-linear plots of the time- and spanwise-averaged velocity profile in wall unit. The log law of incompressible flat-plate boundary layer flow, and the log law given by Van Driest(1951), and a first-order theoretical law of the wall given by White and Chrisoph(1972) are also plotted for comparison.

detail in the next section.

1.4.3 Organized motions

Identification of Λ-vortices

During the post-processing of our LES database, there are several possible ways to identify the large-scale vortical structures. The alternative choices include the low pressure, the negative value of the second invariant of velocity gradient tensor, and the peak value of vorticity. It is reported by Sandham & Kleiser (1992) that second invariant appears to be a good measure when the vortices are very weak, and the low pressure can get better results for strong vortical structures. The vorticity has been proved to be problematic, since it can not distinguish between shear layers and vortices. It is also shown by Kleiser & Laurien (1985) that the Λ-vortex does not necessarily consist of a bunch of vortex line. The results of Robinson (1991) demonstrated that vortex lines can give the illusion of hairpin vortices, even when there are no such vortices in a flow. Thus low pressure
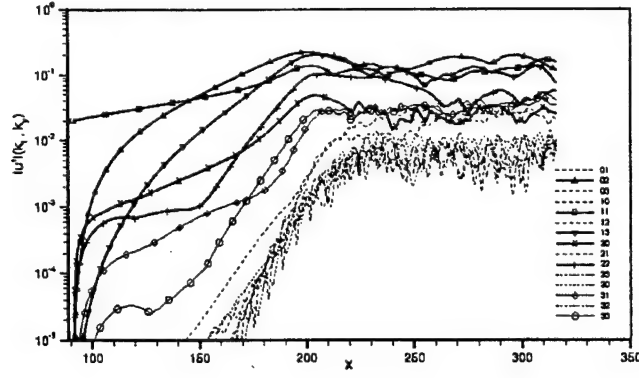
10

Figure 1.6: Spatial growth of the maxima amplitude of streamwise velocity perturbation modes, the even modes are drawn in solid line, and the odd modes in dashed line.

turns out to be the most useful for the identification of vortices than other criteria, especially at highly nonlinear stages(Adams & Kleiser, 1996). In our work, the large-scale vortices are identified by the iso-surface of low pressure. The iso-surface of streamwise vorticity component ω_x is also used as a creteria for comparison. We find out that for large-scale vortical structures, low-pressure tube usually appeared in the core of the vortex. The large-scale vortical structures can be identified precisely through both the low pressure criteria and the concentration of streamwise vorticity. But the results obtained from these two methods diversify when weakly disturbed flow is concerned, where there is no actually physical vortical structure. In this case, although the iso-surface of streamwise vorticity component comes out to be tube-shaped, they can't be interpreted as vortical structures. For example, in our spatial simulation, an oblique wave was imposed at the inlet boundary. Near the inflow boundary, the disturbance experiences a linear and weakly nonlinear growth. In the region between $x \approx 91\delta_{in}$ and $x \approx 180\delta_{in}$, the iso-surface of the streamwise vorticity component appears to be tube-shaped, shown in Figure 1.7. But the low pressure area indicated by iso-surface of pressure in this figure is much different from the vorticity tubes. The conclusion is that the streamwise vorticity component originating from the initially imposed perturbation can not be regarded as the physical vortical structures. It is also quite clear from this figure that the axis of these ω_x iso-surface is parallel to the streamwise direction. So the low-pressure method is by and large superior compared with the vorticity method. Hence, the low pressure will be used to identify the vortical structure.

A further confirmation of the low-pressure method in our results is depicted in Figure 1.8, where the iso-surface of low-pressure ($p = 0.032\rho_\infty U_\infty^2$) is plotted. The low-pressure tubes are cut by two cross-section planes. On each plane, the streamline of cross-flow is drawn as well as the contours of streamwise vorticity. The vortex core marked by the streamline just sites inside the low-pressure tube. In this figure, the concentration of vorticity coincides with the low-pressure part.
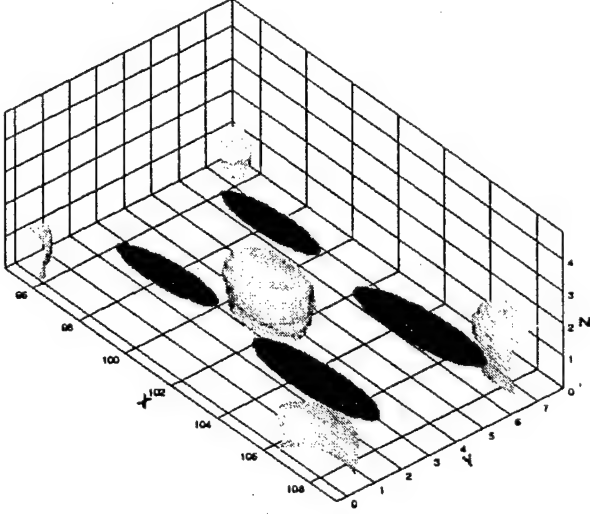
11

Figure 1.7: Iso-surface of streamwise vorticity and low-pressure near the inflow boundary ($\omega_x = \pm 0.06 U_\infty / \delta_{in}$, dark; $p = 0.035 \rho_\infty U_\infty^2$, light)
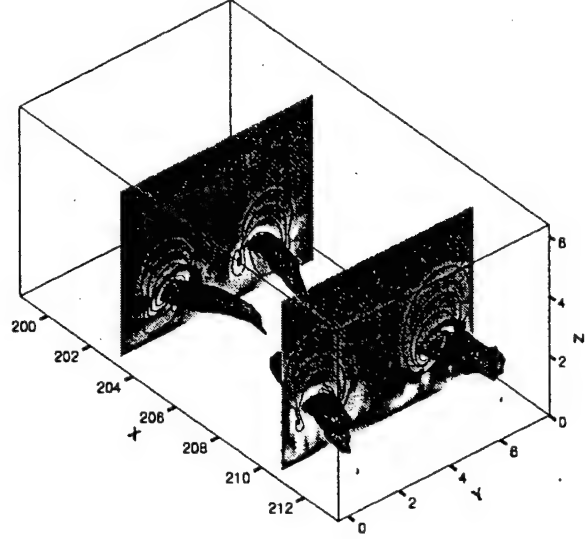
Figure 1.8: Cross flow streamline on a slice normal to the streamwise direction. Iso-surface(wire form) of low pressure $p = 0.032 \rho_\infty U_\infty^2$. Contour of streamwise vorticity plotted on the planes of cross-section

Evolution of Λ-vortices

The Y-shaped shear layers are observed in temporal simulation of subharmonic breakdown(Adams & Kleiser, 1996) and oblique breakdown (Guo *et al.*, 1994). In our results of LES using the spatial approach, the Y-shaped shear layer being displayed by the iso-surface of spanwise vorticity, clearly appears after $x \approx 170\delta_{in}$. The spatial distribution of these Y-shaped shear layers and the Λ-vortices is depicted by a top view in Figure 1.9. The Y-shaped shear layers are staggered in the streamwise direction. On the cross-section it is observed that the rolling-up of the Y-shaped shear layers generates the open-tip Λ-vortices. Looking from the upstream, the right branch of a Y-shaped shear layer rolls down while the left branch of the staggered Y-shaped shear layer downstream rolls up, thus a clockwise rotation of fluid is formed, i.e., a right tail of an open-tip Λ-vortex. Similarly, the left tail of the open-tip Λ-vortex comes from the rolling down of a left Y-branch and rolling up of a downstream staggered right Y-branch. Thus the resulted open-tip Λ-vortices also form a staggered system in the streamwise direction. Because of the deformation and break-up, the stalk of the Y-shaped shear layers disappear after $x \approx 207\delta_{in}$, while the remnant of the Y-branches evolves into the shear layers surrounding the tail of the Λ-vortices.

The appearance of Λ-vortices indicates the start of the second stage of transition. A series of open-tip Λ-vortices between $x = 200\delta_{in}$ and $x = 228\delta_{in}$ are displayed in Figure 1.10. These Λ-vortices are staggered in the streamwise direction. The staggered system of these Λ-vortices
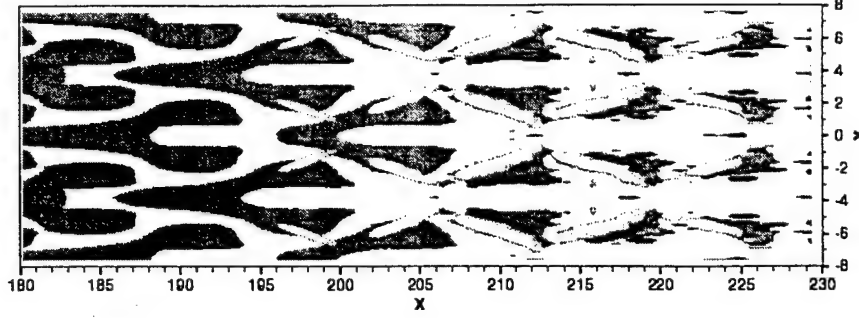
Figure 1.9: Iso-surface of low pressure $p = 0.0315\rho_\infty U_\infty^2$, and iso-surface of spanwise vorticity $\omega_y = 0.68U_\infty/\delta_{in}$. (data duplicated periodically in the spanwise direction).

resembles the scenery of subharmonic secondary instability (H-type) in a flat-plate boundary layer flow. the H-type breakdown is characterized by the appearance of the staggered Λ-vortices. In the case of a subharmonic secondary instability, the inflow perturbation is composed of a two-dimensional primary wave of second-mode and random noise. The wavenumber (k_t, k_y) of the primary mode is $(0, 2)$. Then the subharmonic mode with a wavenumber of $(1, 1)$ grows from the random noise. The strongly nonlinear interactions between the dominant mode lead to the generation of a staggered system of Λ-vortices, whose streamwise repeating distance equals to twice the primary wavelength. Thus streamwise repeating distance is the same as the wavelength of the subharmonic mode.

In our simulation, a pair of oblique first-modes with wavenumber (k_t, k_y) of $(1, 1)$, $(1, -1)$ and equal amplitude are imposed on the upstream boundary to serve as the inflow perturbation. The instability is evoked first by the linear and weakly nonlinear interactions between the oblique modes and the even modes, then by the strongly nonlinear interactions, as a result the odd modes are brought out. As the onset of the strongly nonlinear interactions between the dominant modes, the staggered Λ-vortices appear. The streamwise repeating distance of the Λ-vortices is close to the oblique primary wavelength. Here, the wavenumber of the primary wave is comparable to the wavenumber of the subharmonic mode in H-type instability. Therefore, the Λ vortical structure coming out from the subharmonic secondary instability and from the oblique instability bear some similarity. as it is described by Adams & Kleiser (1993). In their temporal direct numerical simulation for an oblique transition at Mach number 4.5, the building-up of a staggered system of streamwise vortices and Y-shaped shear layers is observed to be similar to the subharmonic transition (Guo *et al.*, 1994). Although the mechanism by which the Λ-vortices are generated is different for the subharmonic instability and oblique instability, the resulted Λ vortical structure is quite similar. It is presumable that after the stage of Λ-vortices, the further development of these two types of transition is similar to each other.

Now we zoom out to include the downstream region of the Λ-vortices (see Figure 1.11). As we have seen before, from $x = 202\delta_{in}$ to $x = 227\delta_{in}$, the tip of the Λ-vortex is lifted by the motion
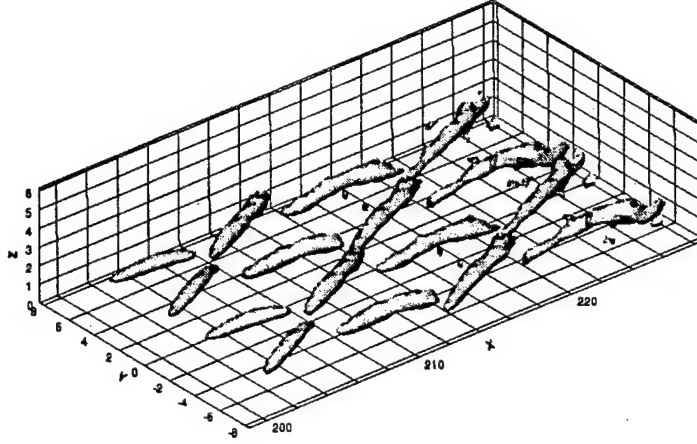
13

Figure 1.10: Iso-surface of low pressure $p = 0.03\rho_\infty U_\infty^2$. (data duplicated periodically in the spanwise direction).

induced by the other tail of the same vortex. Although the lifting angle is quite small (approximately 15°) in this region, the downstream velocity difference caused by the mean shear drives the vortex to stretch considerably in the streamwise direction. As the tip of Λ-vortex sticks out of the strong mean shear layer, the decrease in the wall-normal derivative of the streamwise velocity enhances the inclination of the tips of Λ-vortices. (e.g., $x \approx 234\delta_{in}$, $x \approx 242\delta_{in}$, $x \approx 249\delta_{in}$). The Λ-vortices undergo deformation between $x \approx 227\delta_{in}$ and $x \approx 242\delta_{in}$. It is observed from the side-view of Figure 1.11 that the tips of the Λ-vortex lifts dramatically near $x \approx 234\delta_{in}$, and the vortex breaks into two parts with the tip and tail of the same vortex separating each other. The original tail of the Λ-vortex becomes weak as the the iso-surface of low pressure shrinks. The broken tails can be regarded as the weak vortex torn off from the original Λ-vortex, but they are still visible downstream near $x \approx 244\delta_{in}$. The connection of remnant open-tips of the original Λ-vortex makes it look like the head of a hairpin vortex (near $x \approx 234\delta_{in}$ on Figure 1.11). Near $x \approx 240\delta_{in}$ on Figure 1.11, the vortical structure is more like hairpin vortex rather than the Λ-vortex. At $x \approx 248\delta_{in}$, the Λ-vortices have eventually evolved into the hairpin vortices. The head of the hairpin vortex becomes strong, as the iso-surface of low pressure grows. The legs of the hairpin vortex are now still broken with the head, they seem to be the remnant of the broken tails of the Λ-vortices at $x \approx 230\delta_{in}$ and are still weak. The enclosed angle of the hairpin vortex head is about 53°. The appearance of the hairpin vortex is regarded as the third stage of supersonic boundary layer transition.

Looking from the upstream, the left leg of a hairpin-vortex is corresponding to negative streamwise vorticity, i.e., counterclockwise rotation (e.g., $x \approx 240\delta_{in}$, $y \approx 2\delta_{in}$; $x \approx 248\delta_{in}$, $y \approx 5\delta_{in}$; and $x \approx 248\delta_{in}$, $y \approx -2\delta_{in}$ on Figure 1.11). The right leg with a positive streamwise vorticity indicates a clockwise rotation(e.g., $x \approx 240\delta_{in}$, $z \approx -2\delta_{in}$; $x \approx 248\delta_{in}$, $y \approx 2\delta_{in}$; and $x \approx 248\delta_{in}$, $y \approx -5\delta_{in}$ on Figure 1.11). The small vortices staying close to the leg of hairpin vortices have an opposite sign in streamwise vorticity.
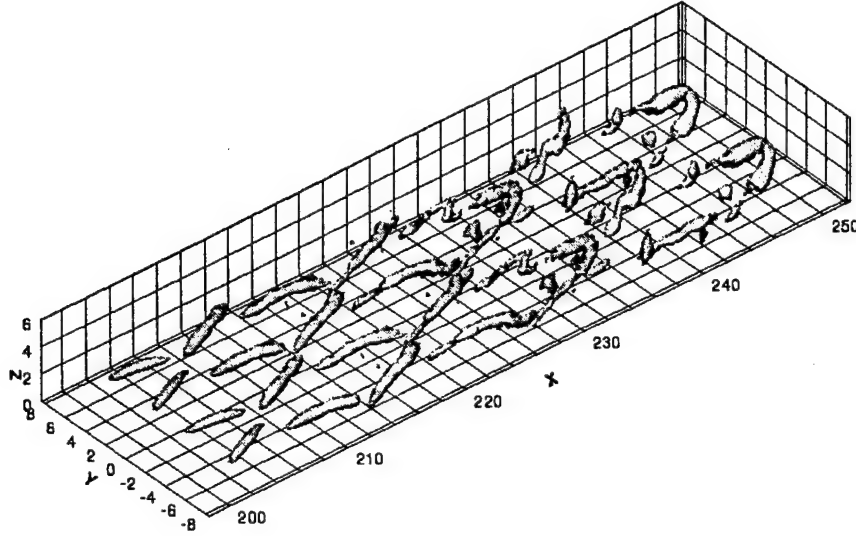
14

Figure 1.11: Iso-surface of low pressure $p = 0.03\rho_\infty U_\infty^2$. (data duplicated periodically in the spanwise direction).

Both vortices and shear layers are interesting flow structures of the transitional and turbulent flow. The Λ-vortices and the evolving hairpin vortices are discribed before this paragraph. Now let us take a look at the shear layers associated with the vortical structures. In Figure 1.12, the contours of the spanwise vorticity ω_y is plotted on a plane cutting through the vortex-tube and a symmetrical plane of the vortex structure. Here the spanwise vorticity ω_y is a good measure to the shear. The shear layers locating away from the wall are produced by the induced motion of the vortical structures.

In order to study the three-dimensional relationship between the shear layers and the vortical structures, the contours of spanwise vorticity is plotted on several cross-sections through $x \approx 200\delta_{in}$ and $x \approx 245\delta_{in}$ in Figure 1.13. It is observed that each tail of a Λ-vortex is wrapped by two high shear regions, i.e., one top layer and one bottom layer. Both the upper and lower shear layers are the branches of the original Y-shaped shear layer shown before in Figure 1.9.

The interactions between the shear layers and the vortical structures are very complex. Generally speaking, the first appearance of the Λ-vortices can be explained as a result of shear layer's rolling up. And new shear layers are generated around the vortices by a process of vortex stretching and convection(Stuart 1965). Usually two types of shear layers are generated by the quasi-streamwise vortical structure, the detached and the attached shear layer. Only the detached shear layer is discribed in the previous paragraph, the attached shear layer is mixed with the mean shear. The attached high-shear layer is visible by plotting the contours of the wall shear stress, as seen in Figure 1.14, where the wall shear stress distribution on the wall in the region between $x = 200\delta_{in}$ and $x = 250\delta_{in}$ is displayed. High wall shear rate corresponding to the attached shear layer can be found close to the outside of the Λ-vortex tail, e.g., $x \approx 222\delta_{in}$, $y \approx -5, -3, 3, 5\delta_{in}$, or $x \approx 228\delta_{in}$,
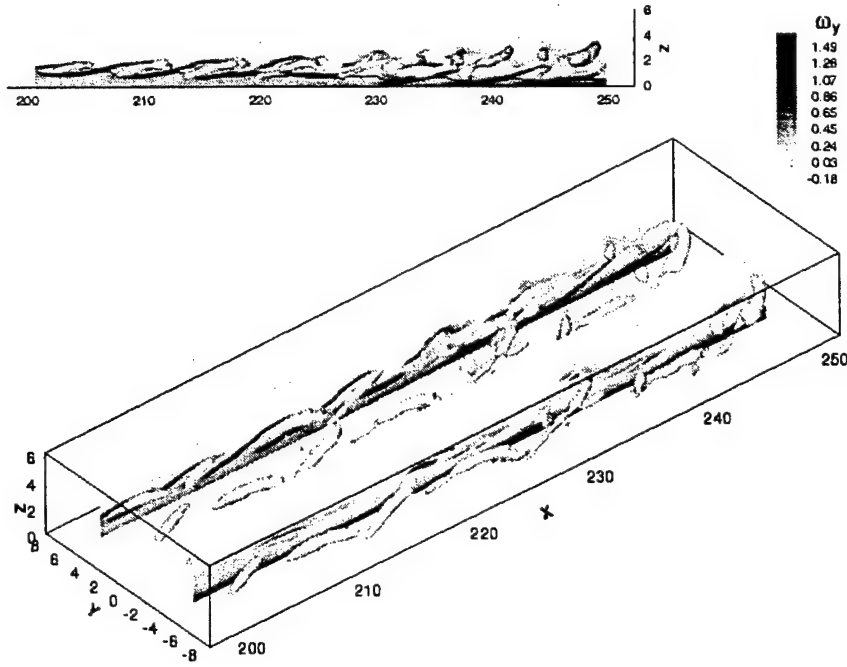
Figure 1.12: Iso-surface of low pressure $p = 0.03\rho_\infty U_\infty^2$, contours of instantaneous spanwise vorticity on the streamwise-sections. (data duplicated periodically in the spanwise direction).
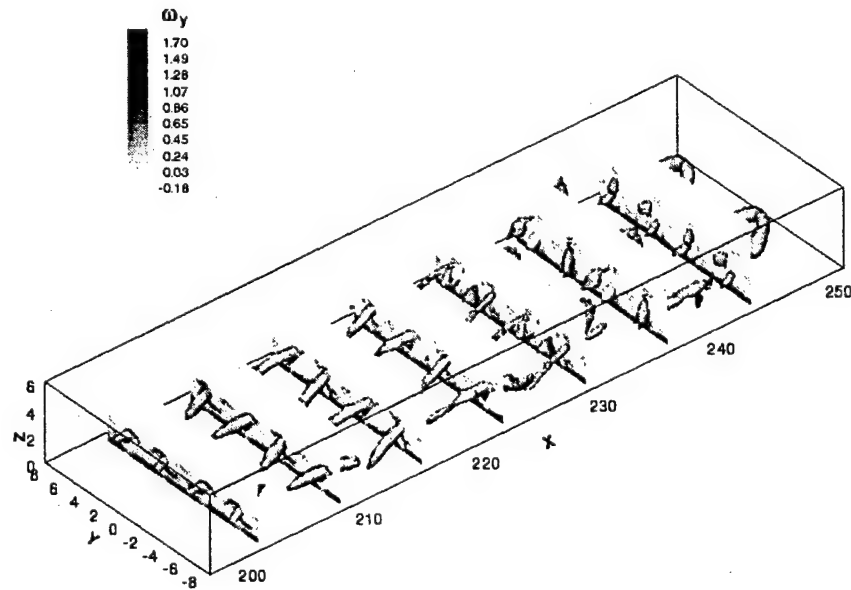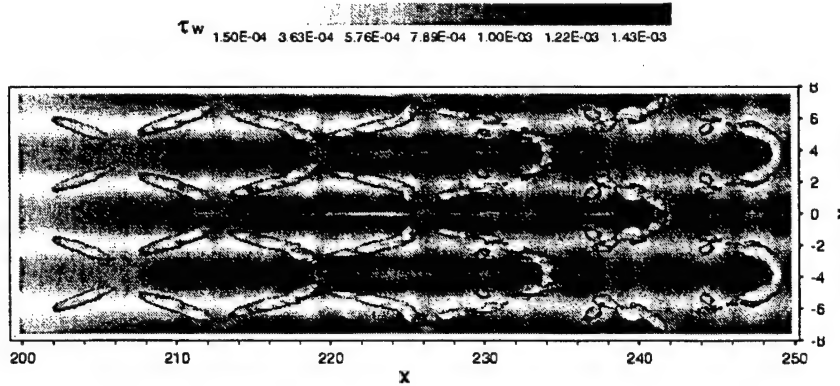

Figure 1.13: Iso-surface of low pressure $p = 0.03\rho_\infty U_\infty^2$, contours of instantaneous spanwise vorticity on the cross-sections. (data duplicated periodically in the spanwise direction).

16

$y \approx -7, -1, 1, 7\delta_{in}$. The attached shear layer is generated by the down-wash motion of fluid toward the wall induced by the vortex tail. The opposite position of these high shear region with respect to the vortex tail is controlled by the up-wash motion, where the wall shear rate is low. The strongest wall shear is discovered between the two tails of the open-tip Λ-vortices or the two legs of the hairpin vortices.

Figure 1.14: Iso-surface of low pressure $p = 0.03\rho_\infty U_\infty^2$, contours of the wall shear stress. (data duplicated periodically in the spanwise direction).

The further development of these hairpin vortices is displayed in Figure 1.15. In this region, the spanwise expansion of the hairpin vortex is quite evident, since the low-pressure areas of adjacent hairpin vortices tend to merge together. Actually the vortices have an opposite rotating direction. A deformation of the hairpin vortices comes out to be visible in this figure, and the legs of the hairpin vortices are stretched in the streamwise direction, as the vortical structure continues to expand in the spanwise direction. The spanwise distance between the left and right legs of the vortex at $x \approx 320\delta_{in}$ reaches $6.4\delta_{in}$. The legs of the hairpin vortices are almost parallel to each other, and also parallel to the wall. Besides the deformation, these hairpin vortices also become weaker as the low-pressure areas shrink. The head of the vortical structures are almost invisible. The broken of these hairpin vortices may lead to the generation of some small scale structures near the head of the former hairpin vortices. But they are not observed clearly in our simulation, which may be blamed to lack of resolution in this region. Further high-resolution DNS may be required. The visible structures left after the breakdown are the streamwise vortices which are located very close to the wall. They evolve from the legs of the former hairpin vortical structure.

1.5 Conclusions

The transition process in a Mach number 4.5 flat-plate boundary layer is investigated by large eddy simulation using the spatial approach. A pair of oblique first-mode perturbation is imposed at the inflow boundary, and the initial field is a laminar boundary layer flow.
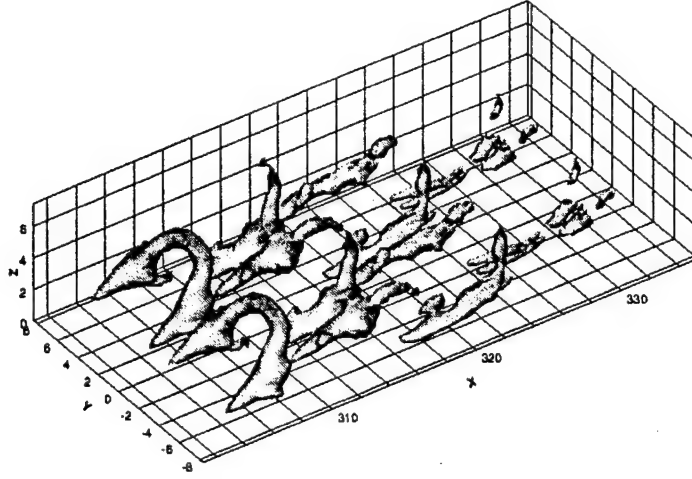
Figure 1.15: Iso-surface of low pressure $p = 0.03\rho_\infty U_\infty^2$. (data duplicated periodically in the spanwise direction).

The linear and weakly nonlinear growth region covers from $x \approx 91\delta_{in}$ to $x \approx 170\delta_{in}$. The spatial growth rate of the primary wave remains at the linear value until $x \approx 170\delta_{in}$. Because the primary wave is composed of a pair of oblique modes $(1, 1)$ and $(1, -1)$, only the 'even' modes(with an even sum of wavenumbers $k_t + k_y$) can be excited through the weakly nonlinear interaction.

The strongly nonlinear interaction occurs after $x \approx 170\delta_{in}$, which is characterized by the appearance of a staggered system of Λ-vortices and Y-shaped shear layers. The 'odd' modes (with an odd sum of wavenumbers $k_t + k_y$) are evoked by the strongly nonlinear interaction.

Shear layers and vortices are the two major structures in the transitional and turbulent flow. Typical Λ-vortices are visible between $x \approx 180\delta_{in}$ and $x \approx 226\delta_{in}$. The vortex core of the Λ-vortices are wrapped by the branches of the Y-shaped shear layers. The induced motion of each tail working on the other gives the inclined nature of the vortices. In the downstream part of this region, the deformation of the Λ-vortices and the Y-shaped shear layers are observed. As a result of the interaction between the self induced motion and the mean shear, deformation occurs to the Λ-vortices and the Y-shaped shear layers.

The next stage of transition is characterized by the appearance of the hairpin vortices, which first appear at $x \approx 248\delta_{in}$. The hairpin vortices are evolved from the deformation of the open-tip Λ-vortices. The further growth of the hairpin vortices is observed downstream, where the spanwise scale of the hairpin is extended with increased inclination. The hairpin vortices are matured near $x \approx 300\delta_{in}$ where the strength of the vortex reaches a maximum. After $x \approx 310\delta_{in}$, the hairpin vortices experience a considerable deformation. the legs stretch in streamwise direction and evolve into the streamwise vortices parallel to the wall. The heads of the hairpin vortices become weak, which is denoted by a thin or discontinued strand of low pressure.

18

The tails of the Λ-vortices and the legs of the hairpin vortices generate detached shear layers as well as high wall shear. The detached shear layers roll up into new vortices.

The above results are in good agreement with the direct numerical simulation both with a temporal approach (Adams & Kleiser, 1996) and a spatial approach (Zhao el, 1997). Compared with our previous DNS work (Zhao el, 1997), fewer grid nodes and computational time are required by LES, but the transitional process is simulated accurately. The mean flow features including the skin friction coefficient, log law distribution of mean velocity are agreed well with the theoretical results. Most of the important organized structures are also observed in the LES data base, which is helpful to the understanding of the basic mechanism of the flow transition. This approach has also been applied to the LES of supersonic and subsonic flow around airfoils, as it will be reported later.

Chapter 2

Compressible Flow Around Two-Dimensional Airfoil

2.1 Two-Dimensional Grid Generation

An elliptic grid generation method first proposed by Spekreuse (1995) is used to generate 2D grids. The elliptic grid generation method is based on a composite mapping, which is consisted of a nonlinear transfinite algebraic transformation and an elliptic transformation. The algebraic transformation maps the computational space $\mathcal{C}$ onto a parameter space $\mathcal{P}$, and the elliptic transformation maps the parameter space on to the physical domain $\mathcal{D}$. The computational space, parameter space, and the physical domain are illustrated in Figure 2.1.
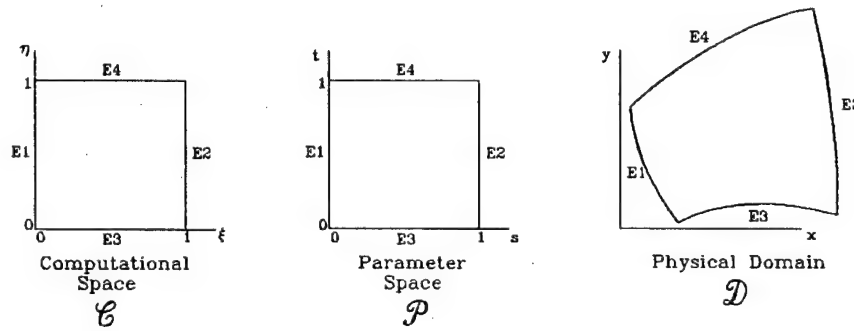
Figure 2.1: Computational space C, Parameter space P, and Physical domain D

The computational space $\mathcal{C}$ is defined as the unit square in a two-dimensional space with Cartesian coordinates (ξ, η), and $\xi \in [0, 1]$, $\eta \in [0, 1]$ (see Figure 2.1). The grids are uniformly distributed on the boundaries and in the interior area of the computational space. The mesh sizes are $\frac{1}{N_\xi - 1}$ in the ξ direction and $\frac{1}{N_\eta - 1}$ in the η direction, where N_ξ and N_η are the grid numbers in the corresponding direction. The parameter space $\mathcal{P}$ is defined as a unit space in a two-dimensional space with Cartesian coordinate (s, t), and $s \in [0, 1]$, $t \in [0, 1]$. The boundary values of s and t are determined by the grid point distribution in the physical domain.

20

- $s = 0$ at edge E_1 and $s = 1$ at edge E_2

- s is the normalized arclength along edges E_3 and E_4

- $t = 0$ at edge E_3 and $t = 1$ at edge E_4

- t is the normalized arclength along edges E_1 and E_2

An algebraic transformation $s : \mathcal{C} \to \mathcal{P}$ is defined to map the computational space $\mathcal{C}$ onto the parameter space $\mathcal{P}$. The grid distribution is specified by this algebraic transformation, which depends on the prescribed boundary grid point distribution. The interior grid point distribution inside the domain, generated by the algebraic transformation, is a good reflection of the prescribed boundary grid point distribution. Let $s_{E_3}(\xi) = s(\xi, 0)$ and $s_{E_4}(\xi) = s(\xi, 1)$ denote the normalized arclength along edges E_3 and E_4, $t_{E_1}(\eta) = t(0, \eta)$ and $t_{E_2}(\eta) = t(1, \eta)$ denote the normalized arclength along edges E_1 and E_2. The algebraic transformation $s : \mathcal{C} \to \mathcal{P}$ is defined as

$$
\begin{aligned}
s &= s_{E_3}(\xi)(1-t) + s_{E_4}(\xi)t \\
t &= t_{E_1}(\eta)(1-s) + t_{E_2}(\eta)s
\end{aligned}
\tag{2.1}
$$

Equation (2.1) is called the algebraic straight line transformation. It defines a differentiable one-to-one mapping because of the positiveness of the Jacobian: $s_\xi t_\eta - s_\eta t_\xi > 0$.

The elliptic transformation $x : \mathcal{P} \to \mathcal{D}$, which is independent of the prescribed boundary grid point distribution, is defined to map the parameter space $\mathcal{P}$ onto the physical domain $\mathcal{D}$. The elliptic transformation is equivalent to a set of Laplace equations

$$
\begin{aligned}
s_{xx} + s_{yy} &= 0 \\
t_{xx} + t_{yy} &= 0
\end{aligned}
\tag{2.2}
$$

The elliptic transformation defined by the above equations is also differentiable and one-to-one.

Till now we have defined two transformations, i.e., the algebraic transformation $s : \mathcal{C} \to \mathcal{P}$, and the elliptic transformation $x : \mathcal{P} \to \mathcal{D}$. Because both the algebraic transformation and the elliptic transformation are differentiable and one-to-one. The composition the two transformation is also differentiable and one-to-one, so as to the inverse transformation.

In physical domain, the curvilinear coordinate system satisfies a system of Laplace equations:

$$
\Delta r = 0
\tag{2.3}
$$

where $r = (x, y)^T$. The inherent smoothness of the Laplace operator makes the grids smoothly distributed in the physical domain. Being transformed to the computational space, this Laplace

system becomes a set of Poisson equations. The control functions is determined by the composed transformation according to the following procedures.

First, Eq.(2.2) is transformed into the computational space $\mathcal{C}$:

$$
\begin{aligned}
\Delta s &= g^{11} s_{\xi\xi} + 2g^{12} s_{\xi\eta} + g^{22} s_{\eta\eta} + \Delta\xi s_{\xi} + \Delta\eta s_{\eta} \\
\Delta t &= g^{11} t_{\xi\xi} + 2g^{12} t_{\xi\eta} + g^{22} t_{\eta\eta} + \Delta\xi t_{\xi} + \Delta\eta t_{\eta}
\end{aligned}
\tag{2.4}
$$

where g^{11}, g^{12}, g^{22} are the components of the contravariant metric tensor, which can be calculated from the covariant metric tensor

$$
\begin{aligned}
g^{11} &= \frac{1}{J^2} g_{22} = (\mathbf{r}_{\eta}, \mathbf{r}_{\eta}) \\
g^{12} &= -\frac{1}{J^2} g_{12} = (\mathbf{r}_{\xi}, \mathbf{r}_{\eta}) \\
g^{22} &= \frac{1}{J^2} g_{11} = (\mathbf{r}_{\xi}, \mathbf{r}_{\xi})
\end{aligned}
$$

J is the Jacobian: $s_{\xi} t_{\eta} - s_{\eta} t_{\xi}$. From Eq.(2.2) and (2.4), we have

$$
\begin{pmatrix} \Delta\xi \\ \Delta\eta \end{pmatrix} = g^{11} \mathbf{P}_{11} + 2g^{12} \mathbf{P}_{12} + g^{22} \mathbf{P}_{22}
\tag{2.5}
$$

where

$$
\begin{aligned}
\mathbf{P}_{11} &= \begin{pmatrix} P_{11}^{(1)} \\ P_{11}^{(2)} \end{pmatrix} = -\mathbf{T}^{-1} \begin{pmatrix} s_{\xi\xi} \\ t_{\xi\xi} \end{pmatrix} \\
\mathbf{P}_{12} &= \begin{pmatrix} P_{12}^{(1)} \\ P_{12}^{(2)} \end{pmatrix} = -\mathbf{T}^{-1} \begin{pmatrix} s_{\xi\eta} \\ t_{\xi\eta} \end{pmatrix} \\
\mathbf{P}_{22} &= \begin{pmatrix} P_{22}^{(1)} \\ P_{22}^{(2)} \end{pmatrix} = -\mathbf{T}^{-1} \begin{pmatrix} s_{\eta\eta} \\ t_{\eta\eta} \end{pmatrix}
\end{aligned}
\tag{2.6}
$$

and the matrix $\mathbf{T}$ is defined as

$$
\mathbf{T} = \begin{pmatrix} s_{\xi} & s_{\eta} \\ t_{\xi} & t_{\eta} \end{pmatrix}
\tag{2.7}
$$

Then the Laplace system Eq.(2.3) is transformed to the computational space $\mathcal{C}$:

$$
g^{11} \mathbf{r}_{\xi\xi} + 2g^{12} \mathbf{r}_{\xi\eta} + g^{22} \mathbf{r}_{\eta\eta} + \Delta\xi \mathbf{r}_{\xi} + \Delta\eta \mathbf{r}_{\eta} = 0
\tag{2.8}
$$

Substitute Eq.(2.5) into Eq.(2.8), $\Delta\xi$ and $\Delta\eta$ are replaced by the control functions on the right-hand-side of Eq.(2.5), and we obtain the Poisson equations for the grid generation as follows:

$$
g^{11} \mathbf{r}_{\xi\xi} + 2g^{12} \mathbf{r}_{\xi\eta} + g^{22} \mathbf{r}_{\eta\eta} + (g^{11} P_{11}^{(1)} + 2g^{12} P_{12}^{(1)} + g^{22} P_{22}^{(1)}) \mathbf{r}_{\xi} + (g^{11} P_{11}^{(2)} + 2g^{12} P_{12}^{(2)} + g^{22} P_{22}^{(2)}) \mathbf{r}_{\xi} = 0
\tag{2.9}
$$

22

where the control functions $P_{11}^{(1)}, P_{12}^{(1)}, P_{22}^{(1)}, P_{11}^{(2)}, P_{12}^{(2)}, P_{22}^{(2)}$ are determined by the algebraic transformation, as defined previously in Eq.(2.6).

The elliptic transformation is carried by solving a set of Poisson equations. The control functions are specified by the algebraic transformation only and it is, therefore, not needed to compute the control functions at the boundary and to interpolate them into the interior of the domain, as required in the case for all well-known elliptic grid generation systems based on Poisson systems. The computed grids are in general not orthogonal at the boundary. The algebraic transformation can be redefined to obtain a grid which is orthogonal at the boundary.

We developed a numerical grid generation code based on this method. Any structured grid with four boundary edges can be generated, the orthogonality condition can also be imposed at any edges. The continuity of grid intervals in the interior area is guaranteed by the elliptic equations, while the continuity of grid intervals on the boundary edges is set by users. In order to achieve the best results, the boundary grid distribution usually should be smooth (continuous up to second order of derivative). Here we provide some examples of 2D numerical generation. Figure 2.2 shows the C-grid around a Joukowsky airfoil. The grids near the leading edge and trailing edge are displayed in Figure 2.3, which shows that the smoothness and orthogonality are well maintained. The grid number is 741 in streamwise (ξ) direction and 121 in wall-normal (η) direction.
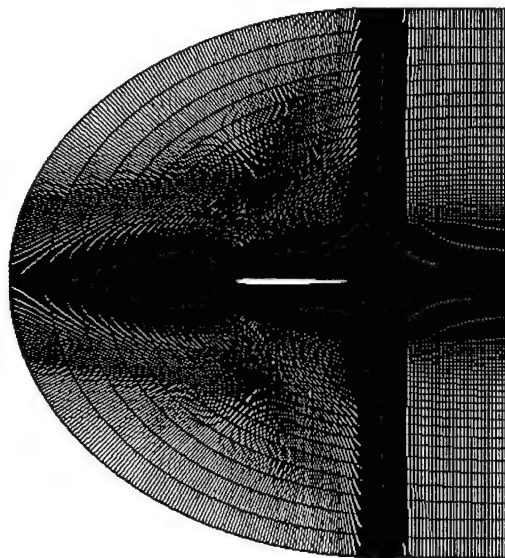

Figure 2.2: C-grid around a Joukowsky airfoil.

In Figure 2.4, the C-grid around a NACA 0012 airfoil is displayed. The grids are orthogonal at the boundaries. The distribution of the grids near the leading-edge and trailing-edge are also depicted by Figure 2.4(c) and (d), where good orthogonality has also been achieved, even though there are two singular points at the trailing-edge. The number of the grids is 601 in the streamwise
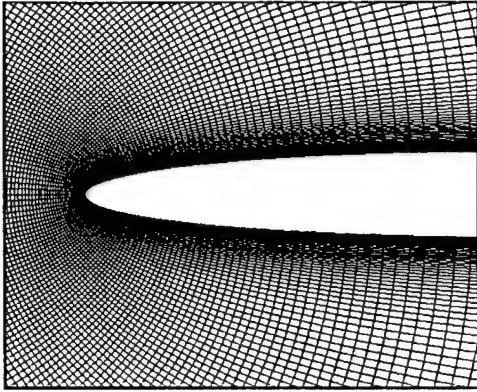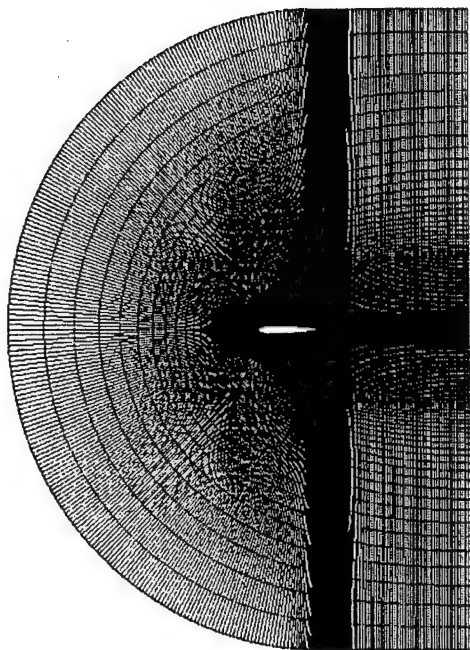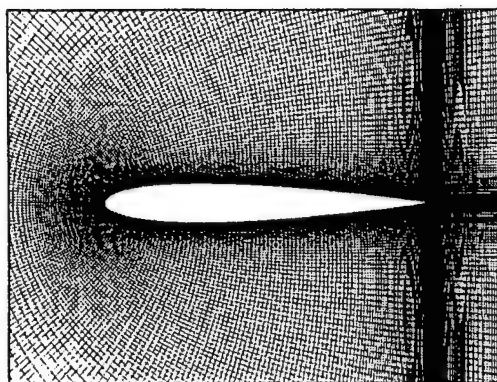
(a)   grids near the leading edge
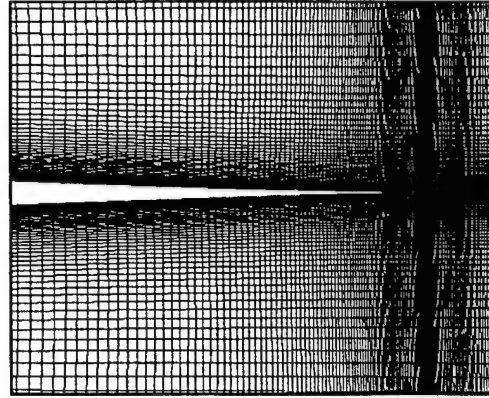
(b)   grids near the trailing edge

Figure 2.3: C-grid near the leading edge and trailing edge of a Joukowsky airfoil. (The grids are orthogonal on the airfoil surface)
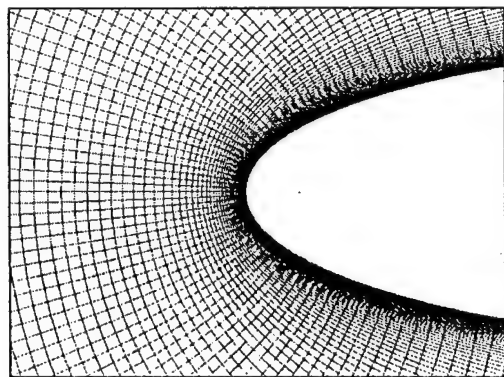
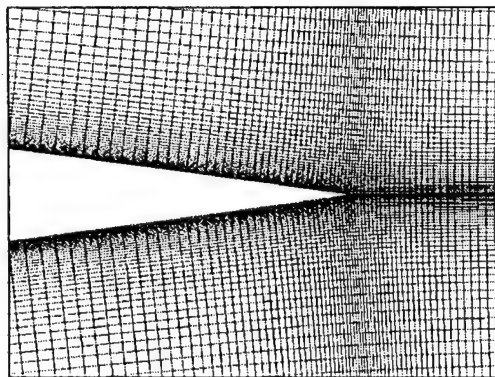(ξ) direction and 121 in the wall-normal (η) direction.

(a) overview of the grids

(b) grid near airfoil surface

(c) grids near the leading-edge

(d) grids near the trailing edge

Figure 2.4: C-grid around a NACA 0012 airfoil

2.2 NACA 0012 Airfoil with a 20° Angle of Attack

The situation of an airfoil with a high angle of attack occurs in many aerodynamic applications which are of particular interest. In these cases, the fluid flow around the airfoil becomes very unstable and eddy structures are formed in the vicinity of the airfoil. These eddy structures lead to modification of the airfoil aerodynamic coefficients which can produce noises. In order to reproduce the unsteady development of the eddy structures in the vicinity of airfoils, a large eddy simulation has been launched for the compressible flow around a NACA 0012 airfoil at a 20 degree angle of attack. The Reynolds number $Re = 5 \times 10^5$, based on the chord length and freestream velocity. The Mach number is $M = 0.4$. A C-grid is generated using the method introduced in the previous section. The grid number is 601 in the ξ-direction and 121 in the η-direction.

The results are shown in Figure 2.5, where the contours of spanwise vorticity at different time are displayed. In the first frame (Figure 2.5(a)), a separation bubble is observed near the leading edge. The leading-edge separation bubble is formed when the laminar boundary layer separates from the surface as a result of the strong adverse pressure gradient downstream of the point of minimum pressure. This minimum-pressure point moves upstream as the angle of attack increases, while the length of the separation bubble decreases (Arena and Mueller, 1980). In our case, the angle of attack is 20 degree, the separation bubble near the leading-edge is very short. Because the separation bubble is very unstable, eddies keep shedding from the leading-edge. Three large scale eddy structures can be observed in Figure 2.5(a). in frame (b) of Figure 2.5, the most downstream eddy reattaches on the airfoil surface. A new shear layer is formed near the surface as a result of the eddy reattachment. In frame (c) the reattached eddy merges with the second and the third eddy, the three vortices is rolling into one big vortex. The induced shear layer evolves into a strong vortex with an opposite rolling direction. The vortex-couple with opposite rolling direction can be observed clearly in frame (e) of Figure 2.5. In the same time, new eddy structure is shedding from the leading-edge separation bubble. The vortex-couple is rolling downstream as shown in frame (e)-(g), until it hits the wake, where some small eddy structures exist. In Figure 2.6, a zoom-in area near the trailing edge is displayed, each frame is corresponding to the same frame in Figure 2.5. In frame (a) of Figure 2.6, instability is observed near the trailing edge. As a result of wake instability, alternate eddy structures are generated in frame (d) and (e). The interaction between the large scale eddy structure, e.g. the vortex-couple and the small scale vortices inside the wake, is displayed through frame (h) to (i) of Figure 2.6. As a matter of fact, the large scale eddy structures overtake the small scale vortices, which disappeared after the interaction, and new large scale vortex is induced.
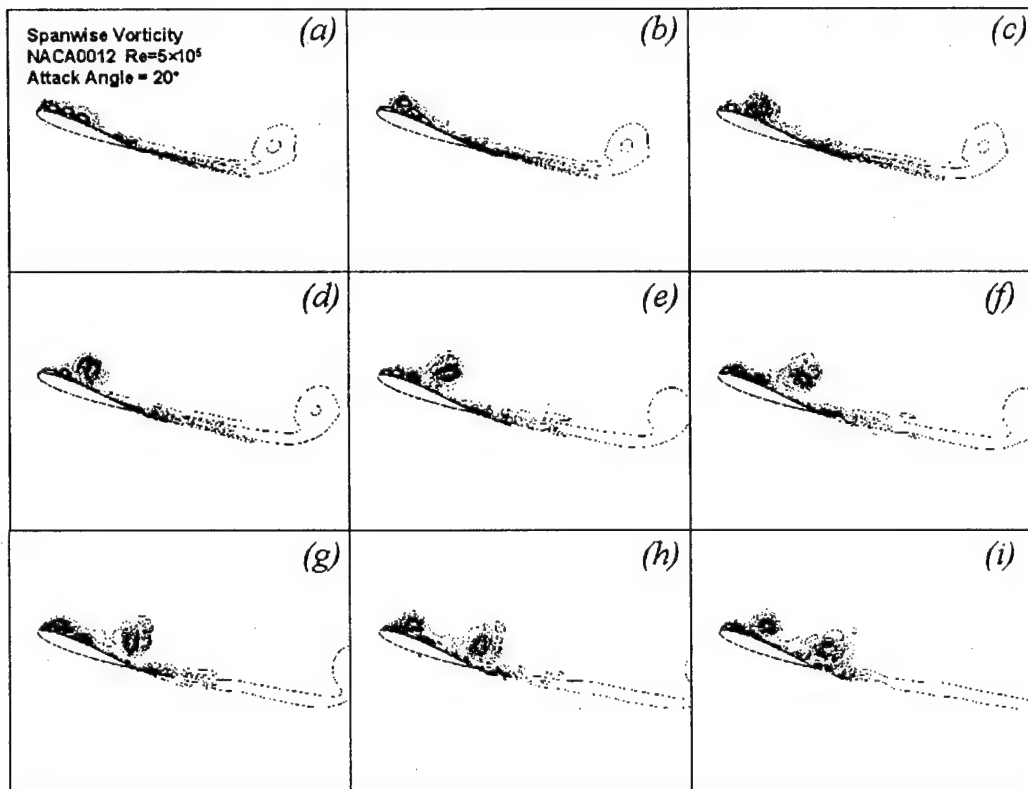
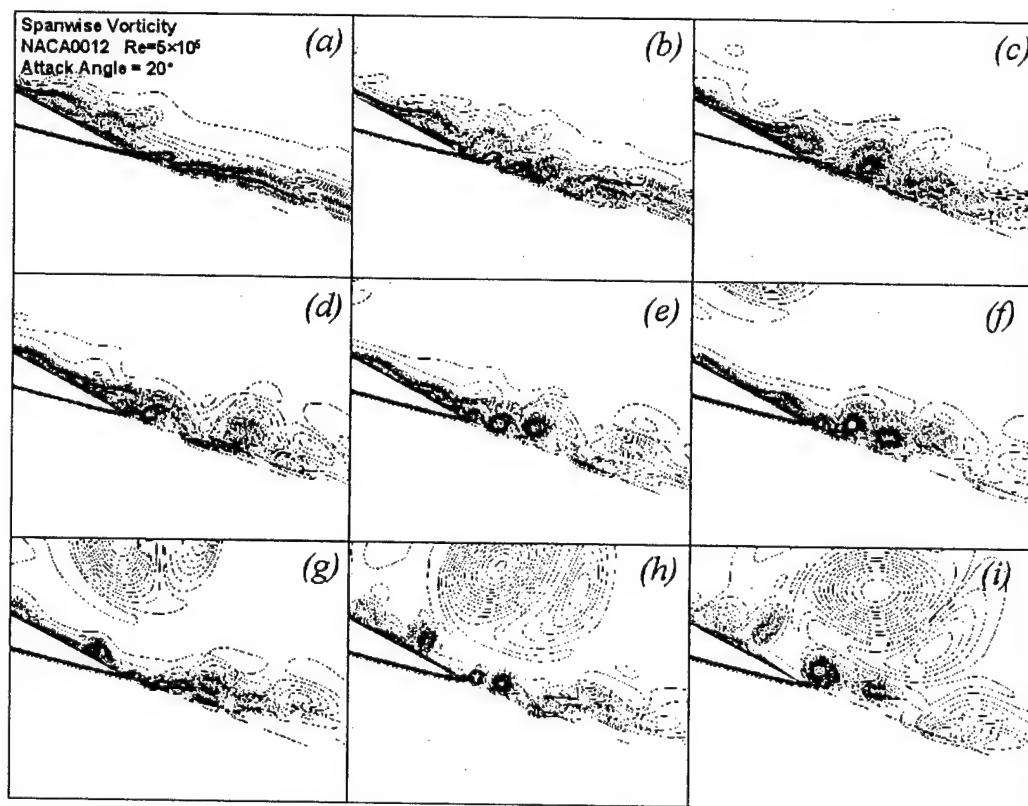Figure 2.5: Contours of spanwise vorticity at different stage

Figure 2.6: Contours of spanwise vorticity near the trailing edge at different stage

Chapter 3

Flow Around Three-Dimensional Airfoil

3.1 Three-Dimensional Grid Generation

The basic idea of three-dimensional grid generation is similar to that of the two-dimensional case. The computational space is a unit cubic with $\xi \in [0,1], \eta \in [0,1], \zeta \in [0,1]$. The parameter space is a unit cubic with $s \in [0,1], t \in [0,1], u \in [0,1]$, see Figure 3.1.

- $s = 0$ at face F_1 and $s = 1$ at face F_2

- s is the normalized arclength along edges E_1, E_2, E_3 and E_4

- $t = 0$ at face F_3 and $t = 1$ at face F_4

- t is the normalized arclength along edges E_5, E_6, E_7 and E_8

- $u = 0$ at face F_5 and $t = 1$ at face F_6

- t is the normalized arclength along edges E_9, E_{10}, E_{11} and E_{12}

Let $s_{E_1}(\xi) = s(\xi,0,0)$, $s_{E_2}(\xi) = s(\xi,1,0)$, $s_{E_3}(\xi) = s(\xi,0,1)$, and $s_{E_4}(\xi) = s(\xi,1,1)$ denote the normalized arclength along edges E_1, E_2, E_3, and E_4; $t_{E_5}(\eta) = t(0,\eta,0)$, $t_{E_6}(\eta) = t(1,\eta,0)$, $t_{E_7}(\eta) = t(0,\eta,1)$, and $t_{E_8}(\eta) = t(1,\eta,1)$ denote the normalized arclength along edges E_5, E_6, E_7 and E_8; $u_{E_9}(\zeta) = u(0,0,\zeta)$, $u_{E_{10}}(\zeta) = t(1,0,\zeta)$, $u_{E_{11}}(\zeta) = u(0,1,\zeta)$, and $u_{E_{12}}(\zeta) = u(1,1,\eta)$ denote the normalized arclength along edges E_9, E_{10}, E_{11} and E_{12}. The algebraic transformation from computational space to parameter space is defined as

$$
\begin{aligned}
s &= s_{E_1}(\xi)(1-t)(1-u) + s_{E_2}(\xi)t(1-u) + s_{E_3}(\xi)(1-t)u + s_{E_4}(\xi)tu \\
t &= t_{E_5}(\eta)(1-s)(1-u) + t_{E_6}(\eta)s(1-u) + t_{E_7}(\eta)(1-s)u + t_{E_8}(\eta)su \\
u &= u_{E_9}(\zeta)(1-s)(1-t) + u_{E_{10}}(\zeta)s(1-t) + u_{E_{11}}(\zeta)(1-s)t + u_{E_{12}}(\zeta)st
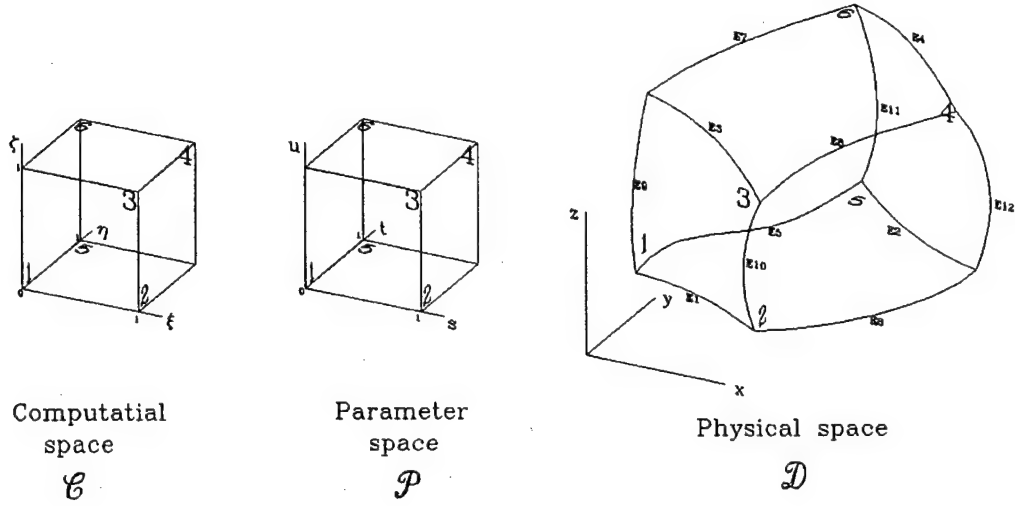\end{aligned}
\tag{3.1}
$$

29

Figure 3.1: Computational space C, Parameter space P, and Physical domain D

Equation 3.1 is called the algebraic straight line transformation.

The Poisson equations for the grid generation are as follows

$$g^{11}r_{\xi\xi} + g^{22}r_{\eta\eta} + g^{33}r_{\zeta\zeta} + 2g^{12}r_{\xi\eta} + 2g^{13}r_{\xi\zeta} + 2g^{23}r_{\eta\zeta}$$
$$+ \quad (g^{11}P_{11}^1 + g^{22}P_{22}^1 + g^{33}P_{33}^1 + 2g^{12}P_{12}^1 + 2g^{13}P_{13}^1 + 2g^{23}P_{23}^1)r_\xi$$
$$+ \quad (g^{11}P_{11}^2 + g^{22}P_{22}^2 + g^{33}P_{33}^2 + 2g^{12}P_{12}^2 + 2g^{13}P_{13}^2 + 2g^{23}P_{23}^2)r_\eta$$
$$+ \quad (g^{11}P_{11}^3 + g^{22}P_{22}^3 + g^{33}P_{33}^3 + 2g^{12}P_{12}^3 + 2g^{13}P_{13}^3 + 2g^{23}P_{23}^3)r_\zeta = 0 \qquad (3.2)$$

where $g^{11}, g^{22}, g^{33}, g^{12}, g^{13}, g^{23}$ are contravariant metric tensor, which are calculated through the covariant metric tensor

$$g^{11} = \frac{1}{J^2}(g_{22}g_{33} - g_{23}^2)$$
$$g^{22} = \frac{1}{J^2}(g_{11}g_{33} - g_{13}^2)$$
$$g^{33} = \frac{1}{J^2}(g_{11}g_{22} - g_{12}^2)$$
$$g^{12} = \frac{1}{J^2}(g_{13}g_{23} - g_{12}g_{33})$$
$$g^{13} = \frac{1}{J^2}(g_{12}g_{23} - g_{13}g_{22})$$
$$g^{23} = \frac{1}{J^2}(g_{12}g_{13} - g_{23}g_{11})$$

where control functions are defined as

$$\mathbf{P_{11}} = -\mathbf{T}^{-1}\begin{pmatrix} s_{\xi\xi} \\ t_{\xi\xi} \\ u_{\xi\xi} \end{pmatrix}, \quad \mathbf{P_{22}} = -\mathbf{T}^{-1}\begin{pmatrix} s_{\eta\eta} \\ t_{\eta\eta} \\ u_{\eta\eta} \end{pmatrix}, \quad \mathbf{P_{33}} = -\mathbf{T}^{-1}\begin{pmatrix} s_{\zeta\zeta} \\ t_{\zeta\zeta} \\ u_{\zeta\zeta} \end{pmatrix}$$

30

$$\mathbf{P_{12}} = -\mathbf{T}^{-1}\begin{pmatrix} s_{\xi\eta} \\ t_{\xi\eta} \\ u_{\xi\eta} \end{pmatrix}, \quad \mathbf{P_{13}} = -\mathbf{T}^{-1}\begin{pmatrix} s_{\xi\zeta} \\ t_{\xi\zeta} \\ u_{\xi\zeta} \end{pmatrix}, \quad \mathbf{P_{23}} = -\mathbf{T}^{-1}\begin{pmatrix} s_{\eta\zeta} \\ t_{\eta\zeta} \\ u_{\eta\zeta} \end{pmatrix} \tag{3.3}$$

and the matrix $\mathbf{T}$ is defined as

$$\mathbf{T} = \begin{pmatrix} s_\xi & s_\eta & s_\zeta \\ t_\xi & t_\eta & t_\zeta \\ u_\xi & u_\eta & u_\zeta \end{pmatrix} \tag{3.4}$$

Figure 3.2 shows the C-H-grid around a 3D delta wing, where the grids on the wing surface and on a $\xi - \zeta$ plane are displayed. We choose C-type for the streamwise direction and H-type for the spanwise direction.
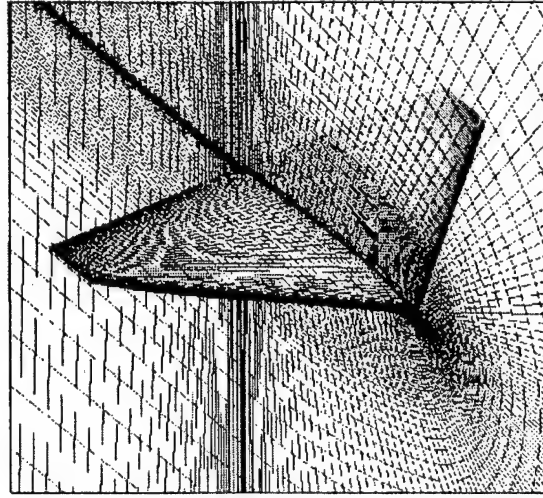
Figure 3.2: C-H-grid around a 3D delta wing.

A set of H-C-grid around a 80° delta wing is generated with the same method. In this case, we choose H-type for the streamwise direction, and C-type for the spanwise direction. The grids are also required to be orthogonal at the boundaries. The grids on selected $\xi - \eta$ sections are displayed in Figure 3.3(a). The grids are orthogonal on delta wing surface and boundaries. Both coarse and fine grid are generated, and the fine grid ($141 \times 70 \times 70$) is shown in Figure 3.3(b).

3.2   3D Delta Wing with a 20° Angle of Attack

Some preliminary results of the large eddy simulation of compressible flow around a 3D delta wing with a 20° angle of attack are obtained. The Reynolds number based on the maximum chord length and the freestream velocity is 5×10^5. March number is $M = 0.4$. The grid number along the ξ-, η- and ζ-direction are 221, 111 and 71, respectively. Here the streamwise, spanwise, and wall-normal
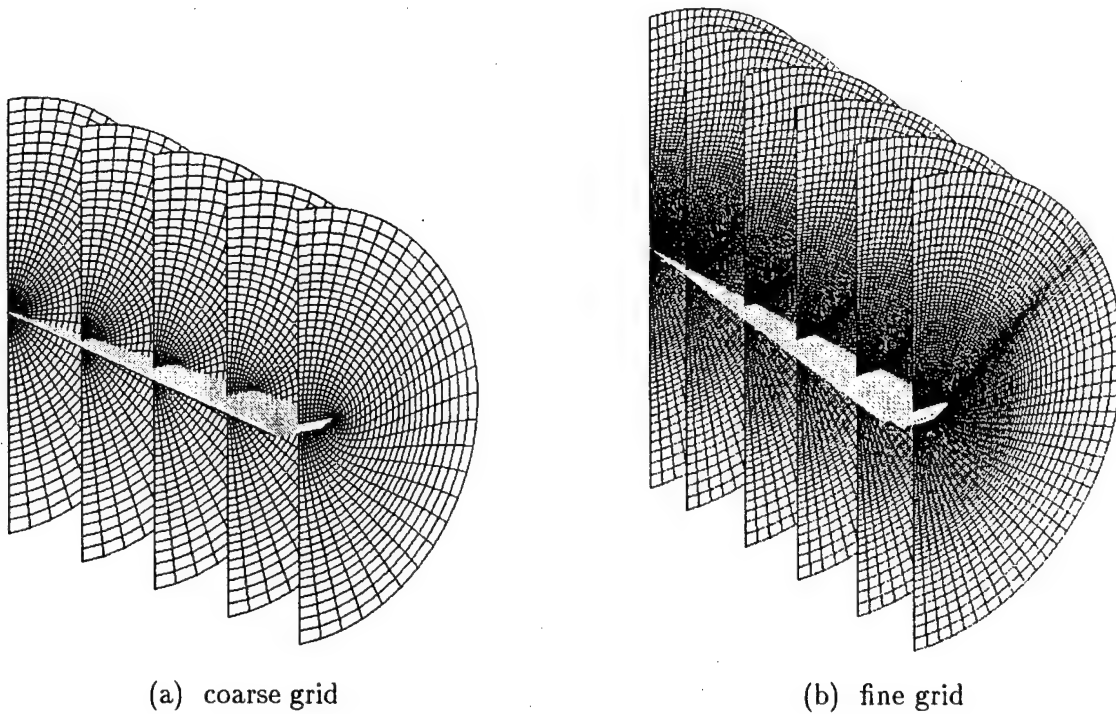
(a) coarse grid   (b) fine grid

Figure 3.3: H-C-grid around a 80° delta wing

directions are denoted by ξ, η, and ζ respectively. The computational domain only contains half of the delta wing and symmetric condition is imposed on the symmetric plane.

In Figure 3.4, the contours of instantaneous pressure on selected $\xi - \zeta$ sections are displayed. The low pressure areas are generally corresponding to flow separation and eddy structures shedding from the wing surface.
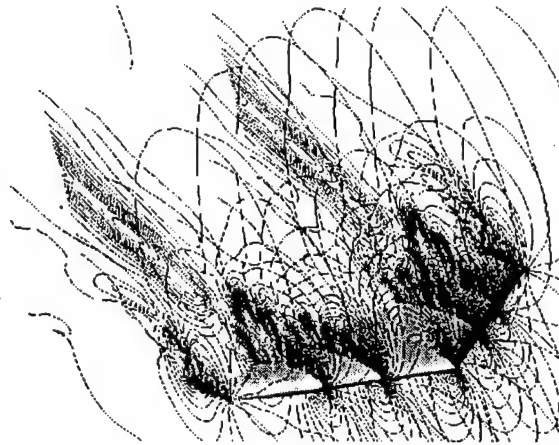
Figure 3.4: Contours of instantaneous pressure on selected $\xi - \zeta$ planes.

Three dimensional streamlines starting from the leading-edge of the delta wing are displayed in

32

Figure 3.5. From this figure, several vortex system can be recognized. A strong streamwise vortex starts from the middle of the wing. This vortex system comes from the separation near the wing surface, and it tends to move outward to the symmetric plane. The wing-tip vortices can also be observed, and it tends to move toward the symmetric plane.
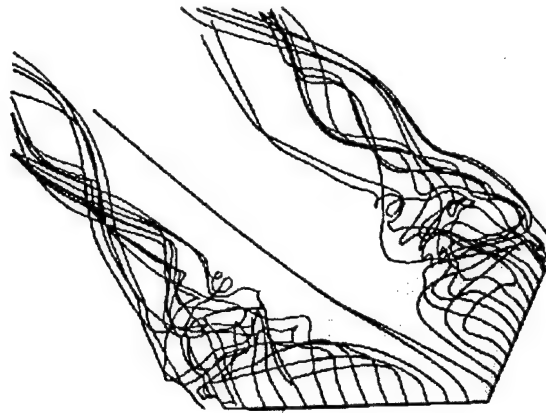

Figure 3.5: 3D streamline starting from the leading-edge

Three components of the vorticity are displayed in Figure 3.6. Again, the separation and shedding of eddy structures near the wing surface can be read from this figure. It is also observed that the vortex system near the wing-tip is very complex and it may require more resolution than we have in this case. The strong streamwise vortices observed in Figure 3.5 is also quite clear by looking at the contours of streamwise vorticity in Figure 3.6(a).
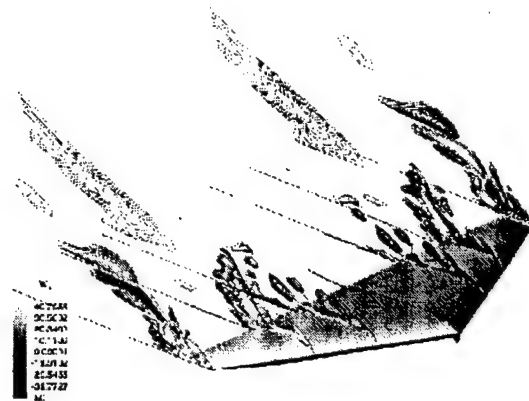
(a) Contours of streamwise vorticity
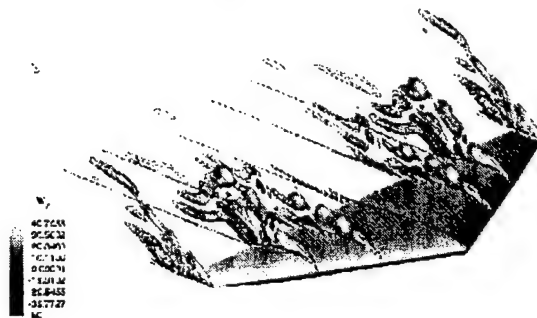
(b) Contours of spanwise vorticity

(c) Contours of wall-normal vorticity

Figure 3.6: Contours of vorticity on selected $\xi - \zeta$ planes.

Aknowledgement

The authors are grateful to AFOSR for the sponsorship to this work. The authors also would like to thank for DoD HPCC for providing computer hours of Cray and other supercomputers.

Bibliography

[1] Adams, N. A., and Kleiser, L. (1993) Numerical simulation of fundamental breakdown of a laminar boundary-layer at Mach 4.5. *AIAA Paper* 93-5027.

[2] Adams, N. A., and Kleiser, L. (1996) Subharmonic transition to turbulence in a flat-plate boundary layer at Mach number 4.5. *J. Fluid Mech.* **317**, pp.301–335

[3] Berlin, S., Lundbladh, A., and Henningson D. (1994) Spatial simulations of oblique transition in a boundary layer. *Phys. Fluids* **6**(6), pp.1949

[4] Chang, C. L., and Malik, M. R. (1993) Non-parallel stability of compressible boundary layers. *AIAA Paper*, 93-2912

[5] Collis, S. S., and Lele, S. K. (1996) A computational approach to swept leading-edge receptivity. *AIAA Paper* 96-0180

[6] Ducros, F., Comte, P. and Lesieur, M. (1996) Large-eddy simulation of transition to turbulence in a boundary layer developing spatially over a flat plate. *J. Fluid Mech.* **326**, pp.1–36

[7] El-Hady, M., Zang, T.A. and Piomelli, U. (1994) Application of the dynamic subgrid-scale model to axisymmetric transitional boundary layer at high speed. *Phys. Fluids* **6**(3), pp.1299–1309

[8] El-Hady, M., Zang, T.A. (1995) Large-Eddy Simulation of Nonlinear Evolution and Breakdown to Turbulence in High-Speed Boundary Layers. *Theoret. Comput. Fluid Dynamics* **7**, pp.217–240

[9] Erlebacher, G., and Hussaini, M. Y. (1990) Numerical experiments in supersonic boundary-layer stability. *Phys. Fluid A*, **2**(1), pp.94–104

[10] Guo, Y., Adams, N. A., Sandham, N. D. & Kleiser, L. (1994) Numerical simulation of supersonic boundary layer transition. In *Application of Direct and Large Eddy Simulation to Transition and Turbulence*, AGARD Conference Proceedings 551, 74th Fluid dynamics Symposium, Chania, Crete, Creece, 1994.

[11] Herbert, Th. and Bertolotti, F. P. (1987) Stability analysis of nonparallel boundary layers. *Bull. Am. Phys. Soc.*, **32**, pp.2079

[12] Herbert, Th. (1988) Secondary instability of boundary layers. *Ann. Rev. Fluid Mech.* **20**, pp.487–562

[13] Laurien, E. and Kleiser, L. (1989) Numerical simulation of boundary-layer transition and transition control. *J. Fluid Mech.* **199**, pp.403-440

[14] Lele, S.K. (1992) Compact finite difference schemes with spectral-like resolution. *J. Comput. Phys.* **103**, pp16–42 Lilly, D. K., (1992) A proposed modification of the Germano subgrid scale closure method, *Phys. FLuids A* **4**, pp.633

[15] Liu, C., and Liu, Z. (1995) Multigrid mapping and box relaxation for simulation of the whole process of flow transition in 3-D boundary layers. *J. Comput. Phys.* **119**, pp.325–341

[16] Liu, Z., Xiong, G., and Liu, C. (1996) Direct numerical simulation for the whole process of transition on 3-D airfoils. *AIAA Paper* 96-2081

[17] Liu, Z., Xiong, G., and Liu, C. (1996) Leading edge receptivity to the freestream vortical disturbance of 2-D and 3-D airfoil. *AIAA Paper* 96-2084

[18] Liu, Z., Zhao, W., Xiong, G., and Liu, C. (1997) Direct numerical simulation of flow transition in high-speed boundary layers around airfoils. *AIAA Paper* 97-0753

[19] Liu, Z., Zhao, W., and Liu, C. (1997) Direct numerical simulation of flow transition in compressible swept-wing boundary layer. In *Proceedings of the First AFOSR International Conference on DNS/LES*, Louisiana Tech University, Rustion, Louisiana, USA, August 4-8, 1997. pp.223–232

[20] Mack, L. M. (1987) Review of linear compressible stability theory. In *Stability for Time Dependent and Spatially Varying Flows*, edited by D.L. Dwoyer and M. Y. Hussaini, Springer-Verlag, New York. pp.164

[21] Moin, P., Squires, K., Cabot, W. and Lee, S. (1991) A dynamic subgrid-scale model for compressible turbulence and scalar transport. *Phys. Fluids A* **3**(11), pp.2746–2757

[22] Ng, L. L., and Erlebacher, G. (1992) Secondary instability in compressible boundary layers. *Phys. Fluids A*, **4**(4), pp.710–726

[23] Normand, X., and Lesieur, M. (1992) Direct and large-eddy simulation of transition in the compressible boundary layer. *Theoret. Comput. Fluid Dyn.* **3**, pp.231–252

[24] Piomelli, U., Zang, T. A., Speziale, C. G., and Hussaini, M. Y. (1990) On the large-eddy simulation of wall bounded shear flows. *Phys. Fluids A*, **2**(2), pp.257–265

[25] Pruett, C. D., Ng, L. L. and Erlebacher, G. (1991) On the nonlinear stability of a high-speed, axisymmetric boundary layer. *Phys. Fluids A*, **3**(12), pp.2910–2926

37

[26] Pruett, C. D. and Zang, T. A. (1992) Direct numerical simulation of laminar breakdown in high-speed axisymmetric boundary layer. *Theoret. Comp. Fluid Dyn.* **7**, pp.49–76

[27] Pruett, C. D., Zang, T. A., Chang, C.-L., and Carpenter, M. K. (1995) Spatial direct numerical simulation of high-speed boundary layer flows-Part I: algorithmic considerations and validation. *Theoret. Comp. Fluid Dyn.*, **7**, pp.49–76

[28] Pruett, C. D., and Chang, C.-L. (1995) Spatial direct numerical simulation of high-speed boundary layer flows-Part II: transition on a cone in Mach 8 flow. *Theoret. Comp. Fluid Dyn.*, **7**, pp.397–424

[29] Sandham, N. D. & Reynolds, W. C. (1991) Three-dimensional simulation of large eddies in the compressible mixing layer. *J. Fluid Mech.* **224,** pp.133–158

[30] Smits, A. J. & Dussauge, J. P. (1996) *Turbulent Shear Layers in Supersonic Flow.* AIP Press, Woodbury, New York.

[31] Spekreijse, S.P. (1995) Elliptic grid generation based on Laplace equations and algebraic transformation. *J. Comp. Phys.*, **118**, pp.38–61

[32] Speziale, C. G., Erlebacher, G., Zang, T. A. and Hussaini, M. Y. (1988) On large eddy simulation of transitional wall-bounded flows. *Phys. FLuids A* **1**, pp.940

[33] Stuart, J. T. (1965) The production of intense shear layers by vortex stretching and convection. *AGARD Rep.* 514

[34] Stuart, J. T. (1984) Instability of laminar flows, nonlinear growth of fluctuations and transition to turbulence. In *Turbulence and Chaotic Phenomena in Fluids* et. T. Tatsumi, Elsevier.

[35] Thompson, J. F., Warsi, Z. U. A., and Mastin, C. W. (1985) *Numerical Grid Generation: Foundations and Applications.* Elsevier, New York, 1985

[36] Thompson, K. W. (1987) Time dependent boundary conditions for hyperbolic systems. *J. Comp. Phys.* **28**, pp.1–24

[37] Thumm, A., Wolz, W., and Fasel, H. (1990) Numerical simulation of spatially growing three-dimensional disturbance waves in compressible boundary layers. In *Laminar Turbulent Transition.* IUTAM Symposium, Toulouse, France, 1989. eds. D. Arnal and R. Michel, Springer-Verlag, Berlin, pp.303–308

[38] Van Driest, E. R. (1951) Turbulent boundary layer in compressible fluids. *J. Aero. Sci.*, **18**, pp.145–160

[39] Van Driest, E. R. (1956) The problem of aerodynamic heating. *Aero. Engrg. Rev.*, **15**(10), pp.26–41

[40] White, F. M., & Christoph, G. H. (1972) A simple theory for the two-dimensional compressible turbulent boundary layer. *J. Basic Engrg.*, **94**, pp.636–642

[41] Wray, A. A. 1986. Very low storage time-advancement schemes. *Internal Report*, NASA-Ames Research Center, Moffet Field, CA.

[42] Zang, T. A., & Hussaini, M. Y. (1990) Multiple paths to subharmonic laminar breakdown in a boundary layer. *Phys. Rev. Lett.* **64**(6), pp.641–644

[43] Zhao, W., Liu, Z., and Liu, C. (1997) Direct numerical simulation of flow transition in a supersonic airfoil boundary layer. In *Proceedings of the First AFOSR International Conference on DNS/LES*, Louisiana Tech University, Rustion, Louisiana, USA, August 4-8, 1997. pp.257–264
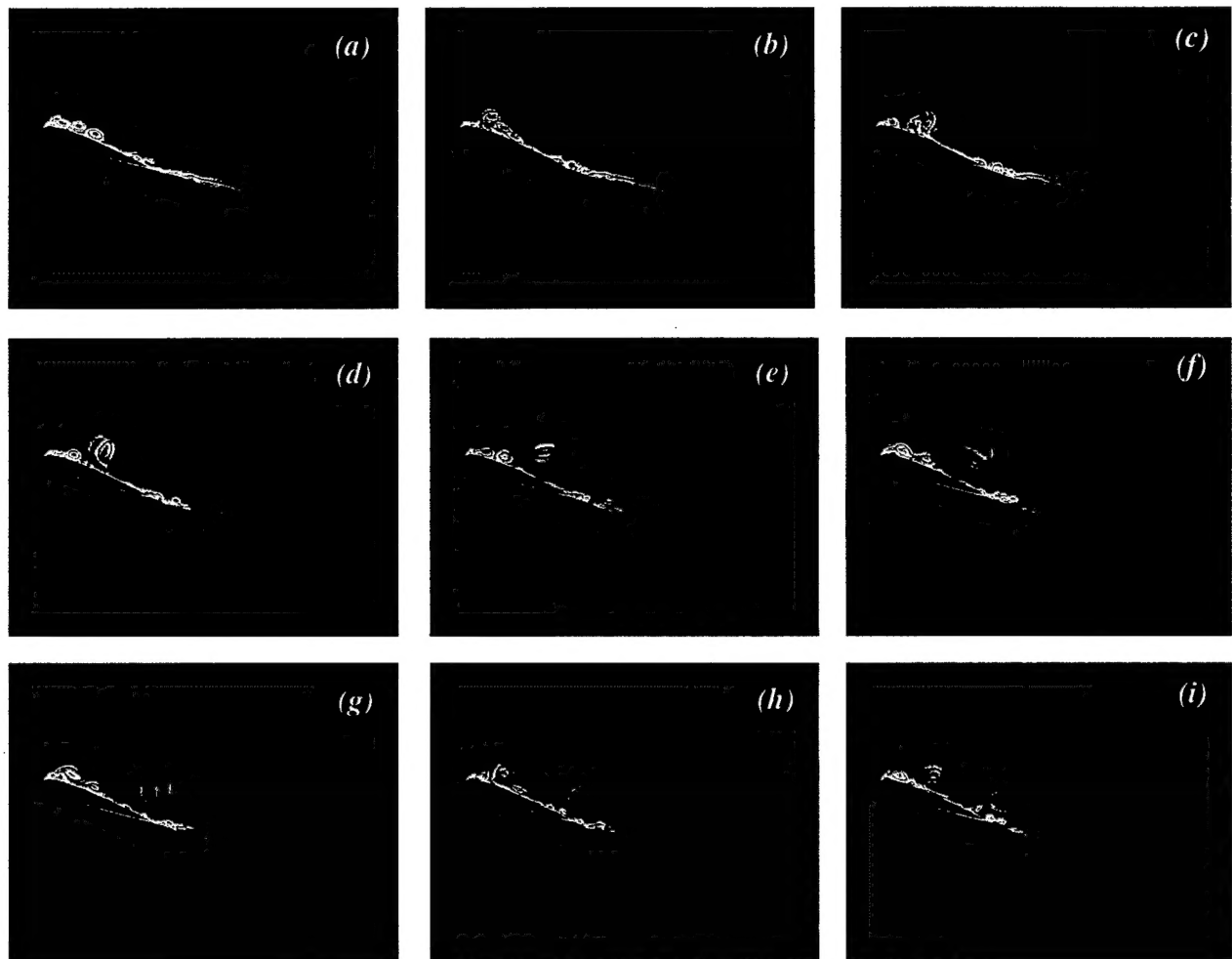
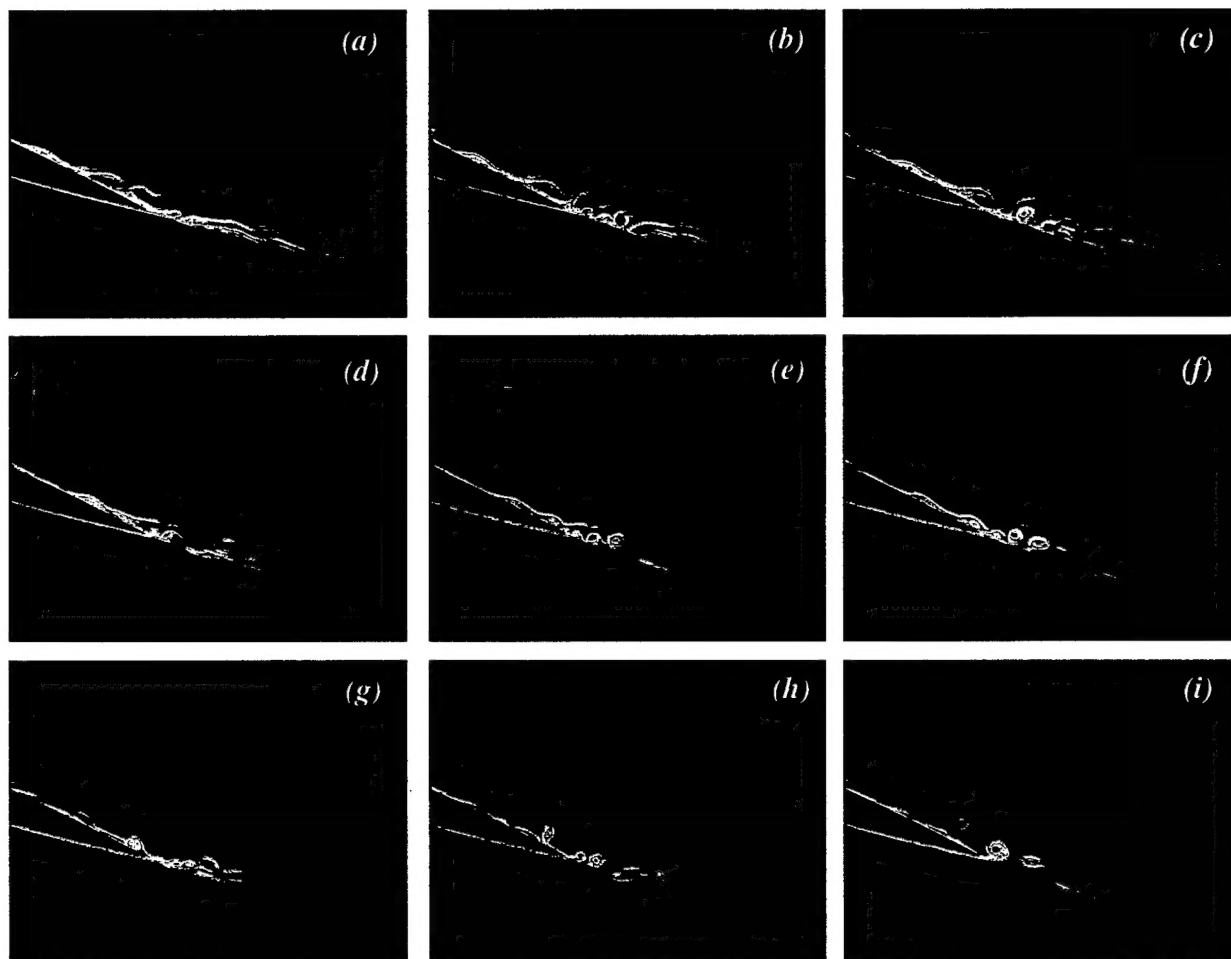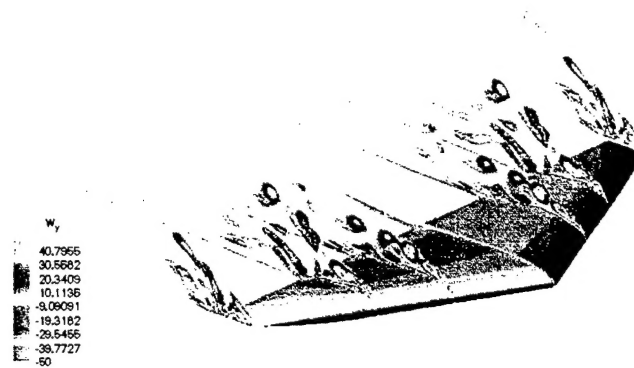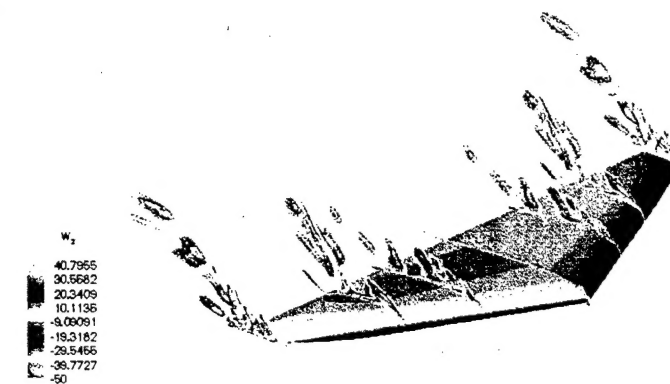Figure 2.5: Contours of spanwise vorticity at different stage

Figure 2.6: Contours of spanwise vorticity near the trailing edge at different stage

(a) Contours of streamwise vorticity

(a) Contours of spanwise vorticity

(c) Contours of wall-normal vorticity

Figure 3.6: Contours of vorticity on selected $\xi - \zeta$ plane